

**$\pi^+p$  backward elastic scattering from 2 to 6 GeV/c**

A. J. Lennox,\* J. A. Poirier, C. A. Rey, and O. R. Sander<sup>†</sup>  
*Department of Physics, University of Notre Dame, Notre Dame, Indiana 46556*<sup>‡</sup>

W. F. Baker, D. P. Eartly, K. P. Pretzl,<sup>§</sup> S. M. Pruss, and A. A. Wehmann  
*Fermi National Accelerator Laboratory, Batavia, Illinois 60510*<sup>||</sup>

P. Koehler\*

*Argonne National Laboratory, Argonne, Illinois 60439*<sup>||</sup>  
 (Received 4 November 1974)

The backward angular distributions obtained in an experiment at the Zero Gradient Synchrotron of Argonne National Laboratory were used to systematically study the energy dependence of the  $180^\circ$  differential cross section for  $\pi^+p$  elastic scattering in the center-of-mass energy region from 2159 to 3487 MeV. At each of 38 incident pion momenta between 2.0 and 6.0 GeV/c, a focusing spectrometer and scintillation counter hodoscopes were used to obtain differential cross sections for typically five pion scattering angles from  $141^\circ$  to  $173^\circ$  in the laboratory. Values for  $d\sigma/d\Omega$  at  $180^\circ$  were then obtained by extrapolation. A resonance model and an interference model were used to perform fits to the energy dependence of  $d\sigma/d\Omega$  ( $180^\circ$ ). Both models led to good fits to our data and yielded values for the masses, widths, parities, and the product of spin and elasticity for the  $\Delta(2200)$ ,  $\Delta(2420)$ ,  $\Delta(2850)$ , and  $\Delta(3230)$  resonances. Our data confirm the existence of the  $\Delta(3230)$  and require the negative-parity  $\Delta(2200)$ .

## I. INTRODUCTION

The energy dependence of  $d\sigma/d\Omega$  at  $180^\circ$  for  $\pi^+p$  elastic scattering shows considerable structure for center-of-mass energies  $\leq 2500$  MeV. However, the higher-energy  $180^\circ$  data points<sup>1-4</sup> available previous to this experiment were too widely spaced to show structure above 2500 MeV. In this experiment we systematically searched for structure in the center-of-mass energy region from 2159 to 3487 MeV by finding  $d\sigma/d\Omega(180^\circ)$  for each of 38 incident pion momenta between 2 and 6 GeV/c. At each of these momenta we obtained angular distributions covering the range  $\sim 163^\circ$  to  $\sim 178^\circ$  in the center-of-mass system and performed fits to the form  $d\sigma/du = [d\sigma/du(180^\circ)] e^{b(u-u_{\max})}$ , where  $b$  is a slope parameter and  $u$  is the square of the crossed four-momentum transfer. The energy dependence of  $d\sigma/d\Omega(180^\circ)$  as well as possible interpretations of the structure observed in the energy dependence have already been reported.<sup>5,6</sup> This paper tabulates the measured angular distributions, gives details of the experimental setup and the method of data reduction, and discusses the models used to fit the energy dependence of  $d\sigma/d\Omega(180^\circ)$ .

## II. EXPERIMENTAL SETUP AND PROCEDURES

## A. Introduction

The beam of pions required for the experiment was produced at the Zero Gradient Synchrotron

(ZGS) of Argonne National Laboratory. A layout of the apparatus used to obtain differential cross sections in the near backward direction is shown in Fig. 1. The incident pions were identified by scintillation counters and three threshold Čerenkov counters. They interacted with protons in a liquid hydrogen target and the reaction products were detected by scintillation-counter hodoscopes. Interactions of interest in this experiment involved the production of a backward pion which entered the backward  $\theta^B$ ,  $\phi^B$  hodoscope and a forward proton which entered the forward  $\theta^F$ ,  $\phi^F$  hodoscope and the focusing spectrometer. For incident pion momenta from 2 to 6 GeV/c, the recoil proton produced in a backward elastic scattering has momentum approximately 300 to 400 MeV/c greater than beam momentum. The spectrometer focused these protons on the momentum hodoscope where they were well separated from the beam pions. A Čerenkov counter just downstream of the momentum hodoscope was used to veto background in which pions entered the hodoscope. This could occur, for example, as a result of scattering from counters or spectrometer magnet pole tips.

Conventional logic circuitry identified events and measured appropriate rates on scalars. Information on the specific combination of counters involved in each individual event was recorded in coincidence registers (latches). Finally, data from the scalars and latches were read into an on-line computer which monitored the experiment and recorded the data on magnetic tape. The re-

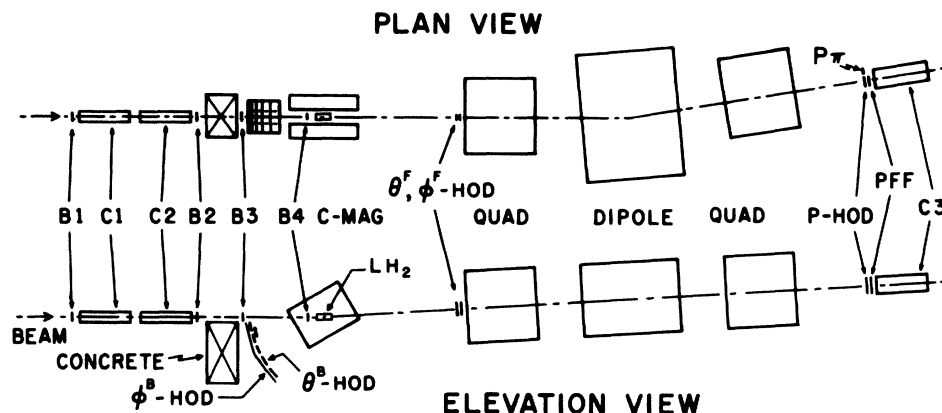


FIG. 1. Experimental layout. The dimensions of the spectrometer for the two geometrical settings are given in Table I.

remainder of this section is devoted to reporting more detailed information on the apparatus itself and the procedures used to obtain the data.

#### B. Experimental layout

The incident pions were produced when a beam of protons extracted from the main ring of the ZGS impinged on a  $10.2 \times 0.64 \times 0.64$  cm<sup>3</sup> beryllium production target. Each beam spill lasted approximately 500 msec and was essentially structureless except for bunching caused by the  $\sim 14.0$  MHz radio frequency in the main ring. The secondary beam line included several bending magnets before the momentum slit and one after the slit. The beam's size and momentum dispersion,  $\Delta P/P$ , could be adjusted by changing the width of this momentum slit. The dispersion was such that 0.63 cm corresponded to 0.5%  $\Delta P/P$ . For most of the data-taking the slit width was  $\sim 2.5$  cm, producing a dispersion of  $\sim \pm 1\%$ . The bending magnet after the momentum slit was used as an analyzing magnet and the absolute value of the momentum was obtained from the magnet's  $7.33^\circ$  bending angle and its  $\int B dl$ , which was measured at a number of current settings spanning the range of our experiment. The systematic error on the central value of the momentum of the beam was estimated to be  $\pm 0.6\%$ . The secondary beam ranged in intensity from  $3 \times 10^5$  to  $4 \times 10^6$  particles per ZGS pulse. The pion content of the beam ranged from 15% at 6 GeV/c to 60% at 2.8 GeV/c.

The following counters were used to identify beam pions: scintillation counters  $B_1$ ,  $B_2$ ,  $B_3$ ,  $B_4$ ,  $AT_1$ , and  $BV_1$ , and Čerenkov counters  $C_1$ ,  $C_2$ , and  $C_4$ . Of these  $B_1$ ,  $B_2$ ,  $B_3$ ,  $B_4$ ,  $C_1$ , and  $C_2$  are shown in Fig. 1. An inverted U-shaped veto counter  $AT_1$  shadowed the top and sides of the target vacuum jacket. The beam-halo veto counter  $BV_1$  was just upstream of the backward hodoscope,

below  $B_3$ . Counter  $C_4$ , which vetoed positrons, was located 27 m upstream of the hydrogen target.  $B_1$  and  $B_2$  were circular with diameter 14 cm and  $B_4$  was circular with diameter 3.8 cm.  $B_3$  was 6.4 cm vertical by 7.6 cm horizontal. Čerenkov counters  $C_1$  and  $C_2$  were 15.2 cm in diameter and 100 cm long. They contained Freon-13 and operated at pressures ranging from 25 to 60 psig depending on the incident beam momentum.  $C_4$  was 10.2 cm in diameter and 100 cm long. It contained Freon-12 and its operating pressures ranged from 3.0 to 14.5 psia.

The hydrogen target flask was cylindrical, 5.1 cm in diameter by 25.4 cm in length, and contained liquid hydrogen at a vapor pressure of  $\sim 13$  psia. Its walls were constructed from one layer of Mylar 0.013 cm thick covered with seven layers of superinsulating material. Each layer of superinsulating material was 0.0006-cm Mylar coated with a layer of aluminum 200 Å thick. The upper and side walls of the vacuum jacket were stainless steel while the bottom and both ends were 0.025-cm-thick Mylar. The Mylar bottom was a necessary feature, permitting the recoil pions to freely enter the backward hodoscope.

The backward scattered pions were located in both azimuthal,  $\phi^B$ , and polar,  $\theta^B$ , angles by a scintillation-counter hodoscope below the incident beam line. Six similar counters, each 22.9 cm wide, separated the pions into six angular bins of  $\theta^B$  from about  $141^\circ$  to  $173^\circ$  in the laboratory. Five of these, designated  $\theta_1^B$  through  $\theta_5^B$ , were placed along the circumference of a circle of radius 137 cm with its center at the center of the hydrogen target as shown in Fig. 1. These five counters were arranged with  $\theta_1^B$  near  $141^\circ$  and  $\theta_5^B$  near  $173^\circ$ . The sixth counter, labeled  $D$ , overlapped  $\theta_5^B$  and  $\theta_4^B$  so as to divide each of them into two smaller bins. Thus, the coincidences  $D \cdot \theta_5^B$  and  $D \cdot \theta_4^B$

along with  $\bar{D} \cdot \theta_5^B$  and  $\bar{D} \cdot \theta_4^B$  subtended polar angles half as large as those subtended by  $\theta_3^B$  through  $\theta_1^B$ . Because the  $\bar{D} \cdot \theta_5^B$  bin extended into the beam halo, the data in this bin were contaminated with beam accidentals and were not included in the analysis. Counters immediately upstream of the  $\theta^B$  counters separated the recoil pions into three bins of  $\phi^B$ . The central counter  $\phi_c^B$  covered the azimuthal angular range  $\pm 5.4^\circ$  from the backward direction;  $\phi_{nc}^{B1}$  extended the range to  $+10.9^\circ$  and  $\phi_{nc}^{B2}$  extended it to  $-10.9^\circ$ . A counter  $T\pi$  located between the hydrogen target and the backward hodoscope indicated that a pion entering the backward hodoscope had originated in the target region.

The forward-going recoil protons were located in azimuth by a counter  $\phi^F$  which was mounted on the upstream end of the first quadrupole magnet in the spectrometer. This counter was narrow (2.54 cm) and limited the  $\phi$  acceptance of the data to scatterings which took place in a nearly vertical plane defined by the trajectories of the incoming pion and the forward recoil proton. Therefore, for elastic events, the backward pions were constrained to fall primarily on  $\phi_c^B$ . The polar scattering angle  $\theta^F$  was divided into seven bins by counters mounted just downstream of  $\phi^F$ . The vertical distance covered by the  $\theta^F$  hodoscope was 21.1 cm, with the bottom of the lowest counter placed 2.6 cm above the beam center line.

The focusing spectrometer separated the forward-going recoil protons from the beam particles and from other scattered particles whose momentum was close to the beam momentum. It consisted of two QM102 quadrupole magnets and a BM109 dipole magnet, with the optical axis pitched vertically to increase the polar angular acceptance. The first quadrupole downstream of the hydrogen target was horizontally defocusing and the second was horizontally focusing. This ar-

angement produced an image of the target which was magnified vertically and reduced horizontally. The dipole magnet, which was located between the two quadrupoles, deflected beam particles  $9^\circ$  horizontally from the nominal beam line. Because of magnet limitations the spectrometer length was increased for beam momenta greater than 4.5 GeV/c. This was accomplished by moving the target, the C magnet, and the backward hodoscope upstream, adjusting the angular orientation of the three spectrometer magnets to obtain a smaller pitch angle, and moving the momentum hodoscope downstream. Data were taken at 4.4 GeV/c and 4.6 GeV/c for both spectrometer lengths so that consistency checks could be made for the two geometries. For taking data at momenta from 2.0 to 4.6 GeV/c the face of the first spectrometer quadrupole was 205 cm from the hydrogen target and the  $\theta^F$  hodoscope mounted on its face accepted protons at polar angles up to  $6.6^\circ$  from the beam line. For momenta from 4.4 to 6.0 GeV/c this distance was increased to 322.6 cm and protons were accepted at angles up to  $4.2^\circ$ . Other parameters describing the two spectrometer geometries are presented in Table I.

Transmissivity measurements and fine-tuning adjustments for the spectrometer were made with the aid of a vertically deflecting dipole C magnet surrounding the hydrogen target. This magnet was used only for adjusting or studying the parameters of the spectrometer and was turned off during normal data-taking. One important adjustment which was made for each beam momentum involved steering the beam so that beam-momentum particles would not enter the momentum hodoscope. This was done by tuning the spectrometer bending magnet in the following manner. The C magnet was used to vertically deflect the beam so as to align it along the spectrometer axis and then the

TABLE I. Spectrometer parameters.

	2.0–4.6 GeV/c operation	4.4–6.0 GeV/c operation
Total length in meters	10.4 m	12.7 m
Vertical pitch angle	$2.58^\circ$	$1.66^\circ$
Vertical acceptance $\Delta\theta_v$	$\pm 45$ mrad	$\pm 29.8$ mrad
Horizontal acceptance $\Delta\theta_h$	$\pm 12$ mrad	$\pm 8.6$ mrad
Momentum resolution $\Delta P/P$	$2.5\%$ <sup>a</sup>	$1.8\%$ <sup>a</sup>
Momentum acceptance $\Delta P/P$	$\sim \pm 30\%$	$\sim \pm 25\%$
Vertical magnification	5.7	4.4
Horizontal magnification	0.17	0.22
Target center to first quad center	2.77 m	3.95 m
Second quad center to hodoscope	2.77 m	3.95 m

<sup>a</sup>Includes the finite size of the momentum hodoscope counters.

current in the bending magnet was adjusted to position the beam on  $P\pi$ , a scintillation counter located at the side of the momentum hodoscope. This counter was 2.54 cm (1.27 cm) wide for the low- (high-) momentum geometry setting. The value of the bending-magnet current obtained in this fashion was then used for normal data-taking with the C magnet turned off and insured the best possible separation of the recoil protons from the beam particles at the momentum hodoscope.

The C magnet was also used to sweep the beam vertically across the  $\theta^F$  hodoscope for transmission studies. During these studies the spectrometer magnets were set to correspond to a momentum on the order of 350 MeV/c lower than the incident beam momentum and the beam was systematically aimed at each of the  $\theta^F$  counters. Thus, during the testing, all the beam particles behaved like recoil protons with momenta higher than the beam momentum. The results of the high-statistics measurements made in this manner agreed with values calculated in a Monte Carlo program to be described later.

The recoil proton momentum hodoscope,  $P$ -HOD, was located at the spectrometer image plane on the high-momentum side of  $P\pi$ . It contained vertical scintillation counters  $P_i^F$ , of 0.63 cm width in front of a vertical counter used in the event trigger,  $PFF$ , 7.7 cm wide. The  $PFF$ ,  $P\pi$ , and  $P_i^F$  counters were each 27.3 cm in height. A Čerenkov counter  $C3$  located just behind the momentum hodoscope was used to discriminate against pions in the hodoscope. This counter was 91 cm long with diameter 30 cm. Its residual counting efficiency for protons was measured so that corrections could be made for accidental vetoes.

### C. Logic circuitry

The logic circuitry was designed to identify events in which a beam pion entered the target, a recoil particle entered the backward hodoscope, and a recoil proton passed through the spectrometer and the momentum hodoscope. Beam pions were identified by the coincidence

$$B1 \cdot B2 \cdot B3 \cdot B4 \cdot C1 \cdot C2 \cdot \overline{(AT1 + C4 + BV1)},$$

defined as  $B\pi$ . The signal  $PF$  indicating that a beam pion had entered the hydrogen target and that a proton from the target had passed through the spectrometer and momentum hodoscope was defined by

$$PF = B\pi \cdot PFF \cdot \phi^F \cdot \overline{(C3 + P\pi)}.$$

The additional requirement that a pion had left the target and entered the backward hodoscope

generated the signal  $\pi B$  defined by

$$\pi B = PF \cdot (\geq 1\theta^B) \cdot T\pi \cdot \overline{BV1}.$$

A coincidence between  $\pi B$  and a signal from one of the counters in the backward  $\phi$  hodoscope generated an event signal which strobed the latches and initiated the transfer of the data to the computer. The event signals  $\pi BE = \phi_c^B \cdot \pi B$  and  $\pi BB = \phi_{nc}^B \cdot \pi B$  distinguished between events where the backward pion entered the central  $\phi^B$  counter and those where it entered one of the outer  $\phi^B$  counters. The delayed  $\pi BE$  strobe, designated  $\pi BEA$ , was used to measure accidental rates. Signals from the  $\theta^F$  and  $P^F$  hodoscopes were recorded in latches and read into the computer, but they were not required in the event strobe.

### D. On-line computer

The experiment was monitored by a Varian Data Machine 620i computer interfaced to coincidence latches and scalars. The on-line program performed its various jobs in the order of their assigned priorities. Highest priority was assigned to reading in the data, performing consistency checks on the data, and finally, recording them on magnetic tape. Lower priority jobs included printing the latch information for each event, printing error messages, and testing the values of the current in each of the magnets downstream of the production target. For the latter job, the computer automatically read the magnet currents, compared their values with a predetermined set of values, and immediately notified the experimenter when a current drifted outside the allowed limits. Lowest priority jobs included a printing or scope display of the scalars or of the ratios of pairs of specified scalars.

## III. DATA REDUCTION

### A. Introduction

Data recorded on magnetic tape for each run included two types of information. The first was the total number of counts occurring in each scaler during the entire run. The second was the latch information, which could be decoded to ascertain the particular combination of counters involved in each individual event. During the data-taking period the scaler information was useful because it enabled the experimenter to quickly identify malfunctioning equipment. However, the correlation information obtained by decoding the latches was used in the off-line data reduction in order to estimate the background and to make appropriate cuts. It was the latched data rather than the data from the scalars that was finally used to calculate a differential cross section for each angular bin.

Two different methods of binning were used to study the  $u$  dependence of the differential cross sections. In the first method the data were organized into bins corresponding to each of the  $\theta^B$  counters; in the second method the bins corresponded to the  $\theta^F$  counters. Both methods produced differential cross sections as a function of  $u$ , but each method involved an independent determination of the  $u$  values at which the cross sections were calculated. In general, the angular distributions thus obtained exhibited an exponential  $u$  dependence. Hence, fits were made to the form  $d\sigma/du = ae^{b(u-u_{\max})}$ , where  $a$  is the value of  $d\sigma/du$  at  $180^\circ$  (the intercept) and  $b$  is the slope parameter. Two fits were made for data taken at each of the 38 incident pion momenta, one for the  $\theta^B$  binning and the second for the  $\theta^F$  binning. For the remainder of this paper the first set of fits will be referred to as the " $\theta^B$  analysis" and the second as the " $\theta^F$  analysis."

#### B. Hodoscope correlation matrices

The first stage of the data reduction process consisted of organizing the latch information into sets of matrices showing correlations among the  $\theta^B$ ,  $\theta^F$ , and  $P^F$  counters. For each value of incident pion momenta two sets of matrices were generated, one set corresponding to data taken with a full target and the other set to empty-target data. In each set the matrix element  $M_{ij}^k$  was the number of events which had triggered the  $k$ th  $\theta^B$  counter, the  $i$ th  $P^F$  counter, the  $j$ th  $\theta^F$  counter, and at least one of the central or noncentral  $\phi^B$  counters. The empty-target subtraction was made by subtracting the appropriately normalized "empty" matrices from the "full" matrices. Visual inspection of the resulting matrices revealed a clear distinction between signal and background. In each matrix the signal was essentially confined to three or four of the  $\theta^F$  bins between  $\theta_1^F$  and  $\theta_5^F$ , inclusive. Cuts on the  $\theta^F$  counters were made by visually scanning the matrices and eliminating the  $\theta^F$  bins which contained only background counts. The number of counts in  $\theta_6^F$  and  $\theta_7^F$  was always small and the contributions from these two counters were not included in the final analysis. Application of the  $\theta^F$  cuts reduced the raw data sample by an amount which varied from 2% to 20%.

The number of counts in a given  $\theta^F$  bin excluded by the cuts was considered to be an estimate of the inelastic background for that particular  $\theta^F$  counter. At a given momentum the background rate (background/number of beam pions) was found to be essentially constant as a function of  $\theta^F$  and  $\theta^B$ . However, the background rate per  $\theta^F$  bin per  $\theta^B$  bin did change smoothly with momentum, ranging from  $9 \times 10^{-10}$  at 2.0 GeV/c to  $2 \times 10^{-10}$  at 6.0 GeV/c.

The correlation between the  $\theta^B$  and  $\theta^F$  counters for an incident pion momentum of 2.8 GeV/c is shown in Fig. 2, which was obtained from the matrices by summing over the  $P^F$  counters, that is, by summing over the index  $i$ . The figure shows the data before the  $\theta^F$  cuts and background subtraction were applied, but after the empty-target subtraction had been made. Similar correlations were observed at all the other incident pion momenta.

By treating the data used to generate Fig. 2 in a slightly different manner it is possible to illustrate the efficiency with which the spectrometer focused the recoil protons. Figure 3 shows the momentum distribution of  $\sim 12\,000$  recoil protons at the momentum hodoscope. These protons were separated from a total of  $\sim 1.1 \times 10^{10}$  positive beam pions which also entered the spectrometer. The histogram was obtained by summing over the  $\theta^F$  and  $\theta^B$  counters, that is, by summing over the matrix indices  $k$  and  $j$  for an incident pion momentum of 2.8 GeV/c. Most of the signal was focused on  $P^F$  counters 3 and 4, while a considerable fraction of the signal in the wings was due to spatial and angular divergences in the beam rather than an aberration of the spectrometer. As is indicated in the figure, events in which the backward pion entered

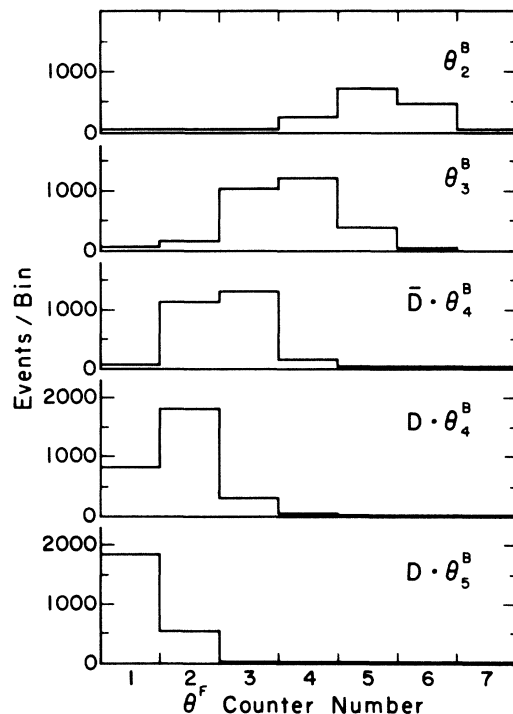


FIG. 2. Correlation between  $\theta^B$  and  $\theta^F$  counters for 2.8 GeV/c beam pions. The figure shows the data after the empty-target subtraction has been made, but before any other cuts or corrections have been applied.

the beam-left  $\phi_{nc}^{B1}$  counter tended to have recoil protons which entered the high-momentum side of the hodoscope, while counts in the beam-right  $\phi_{nc}^{B2}$  counter tended to be correlated with the low-momentum side of the hodoscope. These correlations were not unexpected in view of the spatial and angular divergences known to be present in the beam.

### C. Monte Carlo programs

Geometric efficiencies for the hodoscope counters upstream of the spectrometer were calculated in a Monte Carlo program which generated approximately 500 000 random events at each momentum. In this program the beam was assumed to have a Gaussian momentum distribution while its angular divergence and spatial distribution were constructed to be consistent with values actually measured for these quantities. The  $u$  distribution was chosen to reflect the approximate distribution of  $u$  values seen experimentally so that the Monte Carlo results would better represent the data, both sys-

tematically and statistically. The program generated an event by choosing a beam particle, an interaction point in the target, and a value for momentum transfer,  $u$ . Straightforward kinematic and geometric calculations were then done to determine which  $\theta^F$  and  $\theta^B$  counters (if any) should detect the forward proton and backward pion. At each momentum an appropriate  $u$  range was chosen and divided into fifty bins. The geometric efficiency of each  $\theta^F$  and  $\theta^B$  counter was then calculated for each  $u$  bin. This resulted in two sets of geometric efficiencies for each momentum, one for the  $\theta^B$  analysis and one for the  $\theta^F$  analysis.

The spatial distribution and angular divergences of the beam used as input to the Monte Carlo were based on beam profiles measured using a pair of scintillation counters, photographic film, and a segmented wire ion chamber (SWIC). For each beam-momentum setting a Polaroid film was placed at the spectrometer entrance and exposed to the beam. The resulting pictures provided a continuous monitor of the shape and position of the beam at each incident pion momentum. More detailed studies of the beam were made using two 3-mm-wide scintillation counters to scan the beam at positions 2.54 m upstream and downstream from the hydrogen target. Vertical profiles were obtained at both positions and a horizontal profile was measured at the upstream position. A downstream horizontal profile was obtained using the photographic film information in conjunction with the vertical profile at that position. The four profiles, the results of vertical position correlation studies, and the results of computer studies based on the beam design program TRANSPORT<sup>7</sup> were used to determine the beam's effective focal point,  $ZF$ . The determination of  $ZF$  was made more precise by adjusting its value in the Monte Carlo program until the Monte Carlo prediction for the distribution of backward pions in the  $\phi_c^B$  and  $\phi_{nc}^B$  counters agreed with that observed experimentally. In a similar fashion, the precision in the determination of the beam height was improved by requiring that the slopes of the angular distributions in the  $\theta^F$  and  $\theta^B$  analyses agree within statistical error. Both adjustments were within the experimental errors. Thus, the requirement of consistency between the  $\theta^F$  and  $\theta^B$  analyses as well as the requirement that the Monte Carlo program correctly predict the backward  $\phi$  distribution improved the reliability and accuracy of the Monte Carlo program used to generate geometric efficiencies.

Spectrometer transmissivities were calculated in a second Monte Carlo program, TURTLE.<sup>8</sup> The shape of the calculated transmissivities as a func-

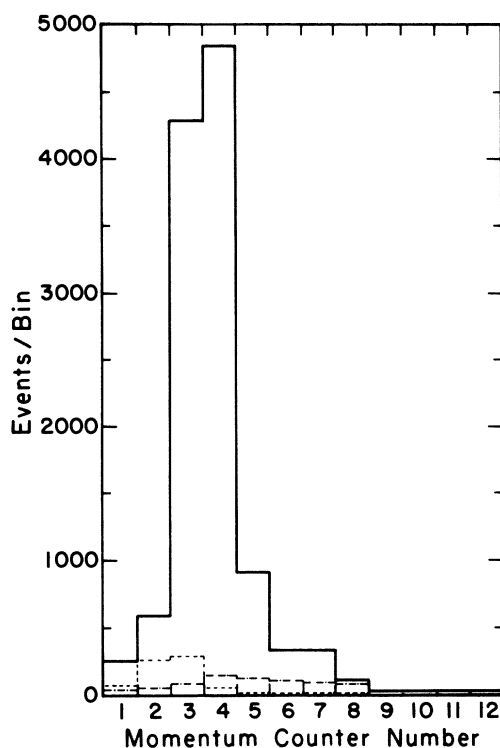


FIG. 3. Momentum distribution at the momentum hodoscope for  $\sim 12\,000$  recoil protons which were separated from  $\sim 1.1 \times 10^{10}$  positive beam pions. The dashed curve represents that subset of recoil protons whose backward pions entered the beam-right  $\phi_{nc}^{B2}$  counter and the dot-dashed curve indicates the number of recoil protons whose backward pions entered the beam-left  $\phi_{nc}^{B1}$  counter. The data sample is the same as that used in Fig. 2.

tion of  $\theta^F$  agreed with the measured transmissivities, and the previously mentioned lack of events in counters  $\theta_5^F$  and  $\theta_7^F$  was also consistent with the predictions of this program. Considering only the five  $\theta^F$  counters used in the analysis, the transmissivities for momenta from 4.6 GeV/c to 6.0 GeV/c were all 100% and for 2.0 GeV/c to 4.6 GeV/c they were a smooth function of  $\theta^F$ , ranging from 87 to 99%. A tabulation of the transmissivities as a function of  $\theta^F$  counters for each momentum is given in Table II.

#### D. Corrections to the data

The largest single correction to the data was necessitated by a defective optical coupling in two of the six  $\phi^B$  hodoscope counters, namely the lower  $\phi_c^B$  and the lower beam-left  $\phi_{nc}^{B1}$  counters. The fact that the  $\phi^B$  hodoscope was included in the trigger requirement caused a loss of events whose backward pion entered the region of overlap between the defective  $\phi^B$  counters and the  $\theta_1^B$ ,  $\theta_2^B$ , and  $\theta_3^B$  counters. Corrections for the inefficiencies were in fact applied to the three  $\theta^B$  bins as though these counters had been partially inefficient. The corrections were generated by demanding consistency between the  $\theta^B$  angular distribution for pions entering the inefficient  $\phi^B$  counters and those entering the beam-right  $\phi_{nc}^{B2}$  counter, which had good optical coupling. The inefficiencies for the two parts of the  $\phi^B$  hodoscope were found to be essentially the same for all of the data. At 3.0 GeV/c the effective efficiency for  $\theta_1^B$  and  $\theta_2^B$  was  $43\% \pm 7\%$  and for  $\theta_3^B$  it was  $55\% \pm 5\%$ . The error bars on the slopes are dominated by the errors associated with this correction. On the other

TABLE II. Spectrometer transmissivities for selected momenta as a function of  $\theta^F$  bins. These values were calculated in the Monte Carlo program, TURTLE.

Momentum (GeV/c)	$\theta_1^F$	$\theta_2^F$	$\theta_3^F$	$\theta_4^F$	$\theta_5^F$
2.0	0.873	0.898	0.914	0.924	0.914
2.5	0.937	0.954	0.974	0.958	0.947
3.0	0.967	0.981	0.986	0.969	0.970
3.5	0.981	0.991	0.985	0.973	0.982
4.0	0.981	0.990	0.981	0.975	0.982
4.5	0.970	0.975	0.980	0.977	0.979
4.7-6.0	1.000	1.000	1.000	1.000	1.000

hand, the values for the cross sections at  $180^\circ$  were essentially unaffected.

Additional corrections included the following: proton absorption in the target, 2%; pion absorption in the target before interaction, 1.5%; inefficiencies in the  $\theta^F$  counters, 3.5%; and multiple counts in the  $\theta^B$  hodoscope, 4%. Pion absorption in the target after an interaction was  $u$ -dependent, ranging from 4.6% for the  $D \cdot \theta_5^B$  bin to 1.3% for the  $\theta_1^B$  bin. An additional 1% correction was applied to the  $D \cdot \theta_5^B$  bin for decay of the backward pion. The correction for accidental vetoes by the  $P\pi$  and C3 counters was beam-rate-dependent and ranged from 2% to 11%. Losses due to  $B\pi$  pile-up were also rate-dependent and ranged from 1% to 4%. Other possible sources of losses which were considered and found to be negligible include multiple Coulomb scattering, accidental events, beam accidentals, and dead times in the  $\theta^B$ ,  $\phi^B$ ,  $\phi^F$ , and  $PFF$  counters.

#### E. Determination of slopes and intercepts

The aforementioned correction factors and the efficiencies calculated in the two Monte Carlo programs were applied to the data in a fitting program called BAKFIT. For each value of incident pion momentum this program generated the angular distributions by calculating the appropriately weighted mean value of  $u$  corresponding to each hodoscope counter and converting the data from each counter to a differential cross section. It then found fits to the form  $d\sigma/du = ae^{b(u-u_{\max})}$  and calculated the best values and the associated errors for the slopes and intercepts. The angular distributions obtained in the  $\theta^B$  analysis are listed in Table III and plotted in Fig. 4. Here the angular distributions for 4.4 and 4.6 GeV/c correspond to the low-momentum geometry; the low-momentum data are presented rather than the high-momentum data because they cover a wider  $u$  range and have better statistical accuracy. The straight lines shown in Fig. 4 are the fits generated by BAKFIT. The angular distributions obtained in the  $\theta^F$  analysis agreed with those from the  $\theta^B$  analysis within statistical error. The consistency between the two analyses is illustrated in Table IV, which compares the slopes and intercepts obtained in both analyses.

For incident pion momenta of 4.4 and 4.6 GeV/c, data were obtained at each of the two spectrometer geometries so that consistency checks could be made. The good agreement between the two settings is shown in Table V, where the slopes and intercepts obtained at the low-momentum geometry (2.0-4.6 GeV/c) are compared with those from the high-momentum geometry (4.4-6.0 GeV/c).

TABLE III. Angular distributions for  $\pi^+p$  backward elastic scattering.

$u$ [(GeV/c) $^2$ ]	$d\sigma/du$ [ $\mu\text{b}/(\text{GeV}/c)^2$ ]	$d\sigma/d\Omega$ ( $\mu\text{b}/\text{sr}$ )	$-\cos\theta_{\text{c.m.}}$	$u$ [(GeV/c) $^2$ ]	$d\sigma/du$ [ $\mu\text{b}/(\text{GeV}/c)^2$ ]	$d\sigma/d\Omega$ ( $\mu\text{b}/\text{sr}$ )	$-\cos\theta_{\text{c.m.}}$
2.0 GeV/c				2.8 GeV/c			
0.155	99.5 $\pm$ 40.5	23.9 $\pm$ 9.7	0.9984	0.115	667.8 $\pm$ 16.8	238.1 $\pm$ 6.0	0.9972
0.150	184.5 $\pm$ 28.0	44.4 $\pm$ 6.7	0.9965	0.110	688.6 $\pm$ 14.1	245.6 $\pm$ 5.0	0.9940
0.142	142.7 $\pm$ 22.7	34.3 $\pm$ 5.5	0.9937	0.101	606.5 $\pm$ 13.6	216.3 $\pm$ 4.8	0.9892
0.129	124.1 $\pm$ 23.0	29.8 $\pm$ 5.5	0.9888	0.083	537.0 $\pm$ 49.7	191.5 $\pm$ 17.7	0.9792
0.114	147.5 $\pm$ 130.1	35.5 $\pm$ 31.3	0.9830	0.058	387.5 $\pm$ 69.1	138.2 $\pm$ 24.6	0.9649
				0.038	122.2 $\pm$ 53.3	43.6 $\pm$ 19.0	0.9537
2.1 GeV/c				2.9 GeV/c			
0.149	59.0 $\pm$ 28.9	14.5 $\pm$ 7.1	0.9984	0.112	534.8 $\pm$ 26.1	198.5 $\pm$ 9.7	0.9970
0.143	91.5 $\pm$ 22.3	22.5 $\pm$ 5.5	0.9962	0.106	593.6 $\pm$ 23.8	220.3 $\pm$ 8.8	0.9936
0.136	70.1 $\pm$ 14.8	17.2 $\pm$ 3.6	0.9931	0.097	486.1 $\pm$ 21.8	180.4 $\pm$ 8.1	0.9887
0.121	92.0 $\pm$ 20.2	22.6 $\pm$ 5.0	0.9873	0.079	406.0 $\pm$ 41.6	150.7 $\pm$ 15.4	0.9782
0.107	39.9 $\pm$ 44.8	9.8 $\pm$ 11.0	0.9815	0.053	292.5 $\pm$ 55.5	108.6 $\pm$ 20.6	0.9626
2.2 GeV/c				3.0 GeV/c			
0.143	158.2 $\pm$ 57.2	42.6 $\pm$ 15.4	0.9982	0.108	413.4 $\pm$ 26.2	159.5 $\pm$ 10.1	0.9968
0.137	275.7 $\pm$ 41.6	74.2 $\pm$ 11.2	0.9959	0.102	411.6 $\pm$ 21.0	158.8 $\pm$ 8.1	0.9934
0.130	232.6 $\pm$ 34.6	62.6 $\pm$ 9.3	0.9926	0.094	382.9 $\pm$ 20.8	147.8 $\pm$ 8.0	0.9883
0.115	204.9 $\pm$ 35.7	55.2 $\pm$ 9.6	0.9864	0.076	284.2 $\pm$ 30.4	109.7 $\pm$ 11.7	0.9776
0.098	145.6 $\pm$ 64.1	39.2 $\pm$ 17.3	0.9794	0.047	234.1 $\pm$ 46.1	90.3 $\pm$ 17.8	0.9599
2.3 GeV/c				3.1 GeV/c			
0.137	559.5 $\pm$ 54.8	158.8 $\pm$ 15.6	0.9980	0.108	103.1 $\pm$ 42.5	39.8 $\pm$ 16.4	0.9424
0.132	539.2 $\pm$ 43.5	153.0 $\pm$ 12.3	0.9956	0.105	297.9 $\pm$ 26.7	119.3 $\pm$ 10.7	0.9968
0.124	524.0 $\pm$ 38.5	148.7 $\pm$ 10.9	0.9921	0.099	307.8 $\pm$ 20.5	123.3 $\pm$ 8.2	0.9932
0.109	354.6 $\pm$ 42.5	100.6 $\pm$ 12.1	0.9855	0.091	298.1 $\pm$ 18.3	119.4 $\pm$ 7.3	0.9880
0.089	228.3 $\pm$ 77.9	64.8 $\pm$ 22.1	0.9766	0.073	250.0 $\pm$ 28.0	100.1 $\pm$ 11.2	0.9766
2.4 GeV/c				3.2 GeV/c			
0.133	935.3 $\pm$ 52.1	279.0 $\pm$ 15.5	0.9979	0.102	274.6 $\pm$ 20.1	114.0 $\pm$ 8.3	0.9967
0.127	732.7 $\pm$ 47.8	218.6 $\pm$ 14.3	0.9954	0.096	230.7 $\pm$ 15.1	95.8 $\pm$ 6.3	0.9930
0.119	611.7 $\pm$ 47.8	182.5 $\pm$ 14.3	0.9918	0.088	210.5 $\pm$ 14.3	87.4 $\pm$ 5.9	0.9875
0.104	495.6 $\pm$ 55.3	147.8 $\pm$ 16.5	0.9846	0.070	162.5 $\pm$ 18.9	67.5 $\pm$ 7.8	0.9758
0.083	306.6 $\pm$ 77.9	91.5 $\pm$ 23.2	0.9747	0.039	138.6 $\pm$ 27.6	57.5 $\pm$ 11.5	0.9555
2.5 GeV/c				3.3 GeV/c			
0.128	964.9 $\pm$ 48.0	301.9 $\pm$ 15.0	0.9978	0.099	178.1 $\pm$ 19.3	76.6 $\pm$ 8.3	0.9965
0.122	821.0 $\pm$ 37.5	256.9 $\pm$ 11.7	0.9951	0.093	195.5 $\pm$ 13.0	84.0 $\pm$ 5.6	0.9926
0.115	809.0 $\pm$ 41.7	253.1 $\pm$ 13.0	0.9912	0.085	178.6 $\pm$ 12.0	76.8 $\pm$ 5.2	0.9869
0.099	596.1 $\pm$ 61.2	186.5 $\pm$ 19.1	0.9834	0.067	161.7 $\pm$ 17.9	69.5 $\pm$ 7.7	0.9746
0.076	336.2 $\pm$ 68.2	105.2 $\pm$ 21.3	0.9723	0.035	135.5 $\pm$ 26.2	58.2 $\pm$ 11.3	0.9529
2.6 GeV/c				3.4 GeV/c			
0.123	789.5 $\pm$ 57.1	258.5 $\pm$ 18.7	0.9975	0.002	53.0 $\pm$ 15.2	22.8 $\pm$ 6.5	0.9310
0.118	938.1 $\pm$ 52.0	307.1 $\pm$ 17.0	0.9947	0.096	174.2 $\pm$ 16.3	77.4 $\pm$ 7.2	0.9962
0.110	716.9 $\pm$ 45.9	234.7 $\pm$ 15.0	0.9906	0.091	168.4 $\pm$ 10.9	74.9 $\pm$ 4.8	0.9922
0.093	587.3 $\pm$ 64.0	192.3 $\pm$ 21.0	0.9820	0.082	153.1 $\pm$ 11.1	68.1 $\pm$ 4.9	0.9863
0.069	441.6 $\pm$ 89.4	144.6 $\pm$ 29.3	0.9696	0.064	126.7 $\pm$ 15.4	56.3 $\pm$ 6.8	0.9734
2.7 GeV/c				3.5 GeV/c			
0.119	798.2 $\pm$ 41.9	273.0 $\pm$ 14.3	0.9974	0.031	95.4 $\pm$ 18.9	42.4 $\pm$ 8.4	0.9504
0.113	821.1 $\pm$ 33.1	280.8 $\pm$ 11.3	0.9943	-0.002	26.2 $\pm$ 11.5	11.6 $\pm$ 5.1	0.9272
0.105	778.4 $\pm$ 33.5	266.2 $\pm$ 11.5	0.9899				
0.087	650.1 $\pm$ 64.7	222.3 $\pm$ 22.1	0.9804				
0.063	572.8 $\pm$ 106.9	195.9 $\pm$ 36.6	0.9671				

TABLE III. (Continued)

$u$ [(GeV/c) <sup>2</sup> ]	$d\sigma/du$ [ $\mu\text{b}/(\text{GeV}/c)^2$ ]	$d\sigma/d\Omega$ ( $\mu\text{b}/\text{sr}$ )	$-\cos\theta_{\text{c.m.}}$	$u$ [(GeV/c) <sup>2</sup> ]	$d\sigma/du$ [ $\mu\text{b}/(\text{GeV}/c)^2$ ]	$d\sigma/d\Omega$ ( $\mu\text{b}/\text{sr}$ )	$-\cos\theta_{\text{c.m.}}$
3.5 GeV/c				4.2 GeV/c			
0.093	167.5±14.4	76.9±6.6	0.9958	0.078	91.9±13.6	51.7±7.7	0.9945
0.088	157.1±11.6	72.2±5.3	0.9916	0.072	101.9±7.4	57.3±4.2	0.9891
0.079	132.6±11.1	60.9±5.1	0.9855	0.063	106.9±8.0	60.1±4.5	0.9812
0.061	112.9±14.2	51.9±6.5	0.9721	0.044	81.6±10.6	45.9±6.0	0.9641
0.027	81.9±17.0	37.6±7.8	0.9476	0.006	57.1±11.9	32.1±6.7	0.9311
-0.007	35.8±12.1	16.4±5.6	0.9233	-0.037	34.3±8.2	19.3±4.6	0.8931
3.6 GeV/c				4.3 GeV/c			
0.091	130.1±16.8	61.7±8.0	0.9958	0.076	100.7±13.2	58.1±7.6	0.9944
0.085	169.4±13.0	80.3±6.2	0.9914	0.070	103.3±9.4	59.7±5.4	0.9888
0.077	107.3±11.6	50.9±5.5	0.9850	0.061	75.2±8.0	43.4±4.6	0.9807
0.058	105.1±14.9	49.8±7.1	0.9711	0.042	64.2±10.0	37.1±5.8	0.9631
0.023	71.2±15.7	33.8±7.4	0.9454	0.004	49.0±11.4	28.3±6.6	0.9292
-0.011	41.6±12.7	19.7±6.0	0.9200	-0.039	26.5±7.4	15.3±4.3	0.8896
3.7 GeV/c				4.4 GeV/c			
0.089	160.3±15.7	78.4±7.7	0.9957	0.075	108.7±9.2	64.4±5.4	0.9942
0.083	129.6±9.5	63.3±4.6	0.9911	0.068	66.7±5.9	39.5±3.5	0.9884
0.074	122.3±8.6	59.8±4.2	0.9844	0.059	70.4±5.3	41.7±3.1	0.9800
0.055	115.2±13.6	56.3±6.6	0.9698	0.040	60.1±7.7	35.6±4.6	0.9619
0.020	82.4±16.5	40.3±8.1	0.9430	0.002	40.7±8.6	24.1±5.1	0.9270
-0.015	47.0±13.5	23.0±6.6	0.9162	-0.042	22.1±5.5	13.1±3.3	0.8853
3.8 GeV/c				4.5 GeV/c			
0.087	165.0±9.7	83.1±4.9	0.9956	0.073	62.4±13.7	37.9±8.3	0.9939
0.081	142.2±6.6	71.6±3.3	0.9908	0.067	72.5±10.3	44.0±6.3	0.9879
0.072	124.6±6.0	62.7±3.0	0.9839	0.058	62.4±6.9	37.9±4.2	0.9794
0.053	101.4±11.2	51.1±5.6	0.9689	0.038	51.4±9.4	31.2±5.7	0.9608
0.017	76.5±14.5	38.5±7.3	0.9408	0.000	39.0±10.3	23.7±6.3	0.9244
-0.019	47.2±10.3	23.8±5.2	0.9120	-0.047	19.5±5.6	11.8±3.4	0.8799
3.9 GeV/c				4.6 GeV/c			
0.084	168.5±11.1	87.3±5.8	0.9953	0.071	82.0±13.0	51.0±8.1	0.9936
0.078	132.5±7.0	68.7±3.6	0.9904	0.065	81.2±6.7	50.5±4.2	0.9875
0.070	112.3±6.6	58.2±3.4	0.9832	0.056	53.9±5.3	33.5±3.3	0.9787
0.050	107.2±12.0	55.6±6.2	0.9677	0.037	46.3±7.0	28.8±4.4	0.9598
0.015	56.8±11.5	29.4±6.0	0.9385	-0.001	30.0±7.2	18.7±4.5	0.9228
-0.024	46.9±10.5	24.3±5.4	0.9075	-0.049	14.8±4.9	9.2±3.0	0.8763
4.0 GeV/c				4.7 GeV/c			
0.082	115.0±12.6	61.3±6.7	0.9950	0.070	70.4±9.6	44.8±6.1	0.9943
0.076	134.9±10.7	71.9±5.7	0.9900	0.064	69.9±5.7	44.5±3.6	0.9878
0.067	94.6±8.7	50.4±4.6	0.9825	0.055	54.6±4.0	34.8±2.5	0.9786
0.048	75.6±10.5	40.3±5.6	0.9666	0.036	45.5±6.3	29.0±4.0	0.9600
0.012	52.3±11.5	27.9±6.1	0.9363	0.007	27.6±7.5	17.6±4.8	0.9309
-0.028	27.8±8.6	14.8±4.6	0.9028	4.8 GeV/c			
4.1 GeV/c				4.9 GeV/c			
0.080	135.0±10.6	74.0±5.8	0.9946	0.069	63.2±7.9	41.2±5.1	0.9940
0.074	124.8±8.4	68.4±4.6	0.9894	0.062	57.6±5.5	37.5±3.6	0.9874
0.065	98.2±6.8	53.8±3.7	0.9818	0.053	49.1±4.5	32.0±2.9	0.9780
0.046	85.3±10.7	46.7±5.9	0.9653	0.034	48.3±6.5	31.5±4.2	0.9585
0.009	63.0±12.7	34.5±7.0	0.9335	0.004	25.6±7.3	16.7±4.8	0.9278
-0.033	37.2±8.3	20.4±4.5	0.8973	4.9 GeV/c			
				0.067	78.9±11.1	52.6±7.4	0.9938
				0.061	58.2±5.9	38.8±3.9	0.9870
				0.052	50.4±4.8	33.6±3.2	0.9775
				0.033	51.1±6.7	34.0±4.5	0.9575
				0.002	23.5±6.1	15.7±4.1	0.9251

TABLE III. (Continued)

$u$ [(GeV/c) <sup>2</sup> ]	$d\sigma/du$ [ $\mu\text{b}/(\text{GeV}/c)^2$ ]	$d\sigma/d\Omega$ ( $\mu\text{b}/\text{sr}$ )	$-\cos\theta_{\text{c.m.}}$	$u$ [(GeV/c) <sup>2</sup> ]	$d\sigma/du$ [ $\mu\text{b}/(\text{GeV}/c)^2$ ]	$d\sigma/d\Omega$ ( $\mu\text{b}/\text{sr}$ )	$-\cos\theta_{\text{c.m.}}$
5.0 GeV/c				5.4 GeV/c			
0.066	65.4 ± 8.8	44.5 ± 6.0	0.9936	0.061	61.4 ± 8.6	45.5 ± 6.4	0.9930
0.060	69.8 ± 6.0	47.5 ± 4.1	0.9868	0.055	46.1 ± 4.4	34.1 ± 3.3	0.9854
0.050	49.3 ± 4.8	33.6 ± 3.3	0.9768	0.045	46.3 ± 4.0	34.3 ± 3.0	0.9745
0.031	42.6 ± 6.4	29.0 ± 4.4	0.9565	0.026	31.2 ± 4.7	23.1 ± 3.5	0.9518
0.000	34.7 ± 9.2	23.6 ± 6.3	0.9227	-0.008	16.1 ± 4.7	11.9 ± 3.5	0.9124
5.1 GeV/c				5.6 GeV/c			
0.065	66.9 ± 6.9	46.6 ± 4.8	0.9935	0.059	49.0 ± 9.5	37.7 ± 7.3	0.9928
0.058	61.8 ± 5.5	43.0 ± 3.8	0.9865	0.052	40.4 ± 4.7	31.1 ± 3.6	0.9848
0.049	43.8 ± 4.3	30.5 ± 3.0	0.9763	0.043	34.9 ± 3.9	26.9 ± 3.0	0.9734
0.030	34.7 ± 5.0	24.1 ± 3.5	0.9554	0.023	24.3 ± 3.9	18.7 ± 3.0	0.9496
-0.002	34.5 ± 8.4	24.0 ± 5.8	0.9204	-0.012	16.6 ± 5.0	12.8 ± 3.9	0.9074
5.2 GeV/c				5.8 GeV/c			
0.064	57.9 ± 6.9	41.1 ± 4.9	0.9934	0.057	48.5 ± 7.1	38.8 ± 5.7	0.9924
0.057	50.7 ± 4.8	36.0 ± 3.4	0.9862	0.050	29.9 ± 4.6	23.9 ± 3.7	0.9842
0.048	37.6 ± 4.3	26.7 ± 3.1	0.9758	0.041	32.5 ± 3.6	26.0 ± 2.9	0.9722
0.029	29.8 ± 4.8	21.2 ± 3.4	0.9545	0.021	23.2 ± 4.3	18.6 ± 3.4	0.9476
-0.004	15.6 ± 4.3	11.1 ± 3.1	0.9183	-0.015	12.5 ± 4.2	10.0 ± 3.4	0.9024
5.3 GeV/c				6.0 GeV/c			
0.062	71.4 ± 7.9	51.8 ± 5.7	0.9932	0.055	34.5 ± 7.1	28.6 ± 5.9	0.9919
0.056	51.1 ± 5.6	37.1 ± 4.1	0.9858	0.048	30.0 ± 4.1	24.9 ± 3.4	0.9834
0.046	37.3 ± 5.4	27.1 ± 3.9	0.9751	0.039	24.5 ± 3.6	20.3 ± 3.0	0.9709
0.027	40.6 ± 6.3	29.5 ± 4.6	0.9531	0.019	17.3 ± 3.4	14.4 ± 2.8	0.9454
-0.006	16.5 ± 6.5	12.0 ± 4.7	0.9153	-0.018	9.8 ± 3.0	8.1 ± 2.5	0.8969

Finally, the averages of the  $\theta^F$  and  $\theta^B$  slopes and intercepts for all 38 incident pion momenta are listed in Table VI and plotted in Figs. 5 and 6. Several interpretations of the structure observed in the energy dependence of the backward cross section (Fig. 6) will be discussed in Sec. IV. The deep dip seen in our data at  $\sim 2.1$  GeV/c is even more evident in

TABLE IV. Comparison of slopes and intercepts obtained in the  $\theta^B$  and  $\theta^F$  analyses at representative momenta.

$P_\pi$ (GeV/c)	$\theta^B$ analysis		$\theta^F$ analysis	
	$\frac{d\sigma}{d\Omega}(180^\circ)$ ( $\mu\text{b}/\text{sr}$ )	Slope [(GeV/c) <sup>-2</sup> ]	$\frac{d\sigma}{d\Omega}(180^\circ)$ ( $\mu\text{b}/\text{sr}$ )	Slope [(GeV/c) <sup>-2</sup> ]
2.0	44.4 <sup>+10.1</sup> <sub>-8.2</sub>	12.9 ± 10.9	43.5 <sup>+9.8</sup> <sub>-8.0</sub>	11.2 ± 10.2
2.5	320.7 <sup>+14.7</sup> <sub>-14.3</sub>	16.7 ± 2.8	293.5 <sup>+13.7</sup> <sub>-13.1</sub>	12.8 ± 2.3
3.0	178.4 <sup>+9.0</sup> <sub>-8.4</sub>	11.7 ± 2.4	176.9 <sup>+8.7</sup> <sub>-8.3</sub>	11.4 ± 2.0
3.5	82.5 <sup>+5.3</sup> <sub>-5.3</sub>	12.9 ± 2.3	85.2 <sup>+5.2</sup> <sub>-5.2</sub>	13.1 ± 2.1
4.0	74.4 <sup>+5.3</sup> <sub>-4.8</sub>	14.0 ± 2.2	75.3 <sup>+5.7</sup> <sub>-5.3</sub>	14.1 ± 2.0
4.5	47.4 <sup>+5.0</sup> <sub>-4.6</sub>	10.3 ± 2.4	50.1 <sup>+5.5</sup> <sub>-5.0</sub>	11.5 ± 2.3
5.0	50.1 <sup>+4.7</sup> <sub>-4.3</sub>	12.8 ± 3.7	54.6 <sup>+5.8</sup> <sub>-5.3</sub>	15.7 ± 3.8
5.6	38.4 <sup>+4.7</sup> <sub>-4.1</sub>	16.0 ± 4.2	38.9 <sup>+5.4</sup> <sub>-4.8</sub>	16.6 ± 4.2
6.0	30.9 <sup>+4.3</sup> <sub>-3.7</sub>	17.6 ± 4.4	31.0 <sup>+4.6</sup> <sub>-4.0</sub>	17.3 ± 3.9

Fig. 7, which contains data from other  $\pi^+p$  backward elastic scattering experiments.<sup>1-4,9</sup> The values plotted in this figure correspond to  $\cos\theta \leq -0.999$ . There is also a vast amount of data<sup>10</sup> for elastic scattering near  $180^\circ$  in the energy region considered in this paper. Because of the rapid change in cross section near  $180^\circ$ , it is difficult to make meaningful comparisons between our data and data corresponding to  $\cos\theta \leq -0.999$ .

#### IV. INTERPRETATION OF EXPERIMENTAL RESULTS

##### A. Introduction

The clear correlation between the peaks observed in the energy dependence of the backward cross section and the position of known resonances has influenced the formulation of several models for backward scattering, including the resonance model and the interference model. In the former model the scattering amplitude for  $\pi^+p$  scattering is written as a sum of Breit-Wigner amplitudes corresponding to resonances having isospin  $I = \frac{3}{2}$ . The latter model also includes Breit-Wigner amplitudes, but superposes these resonant amplitudes on a nonresonant background, which is usually written in terms of a Regge amplitude.

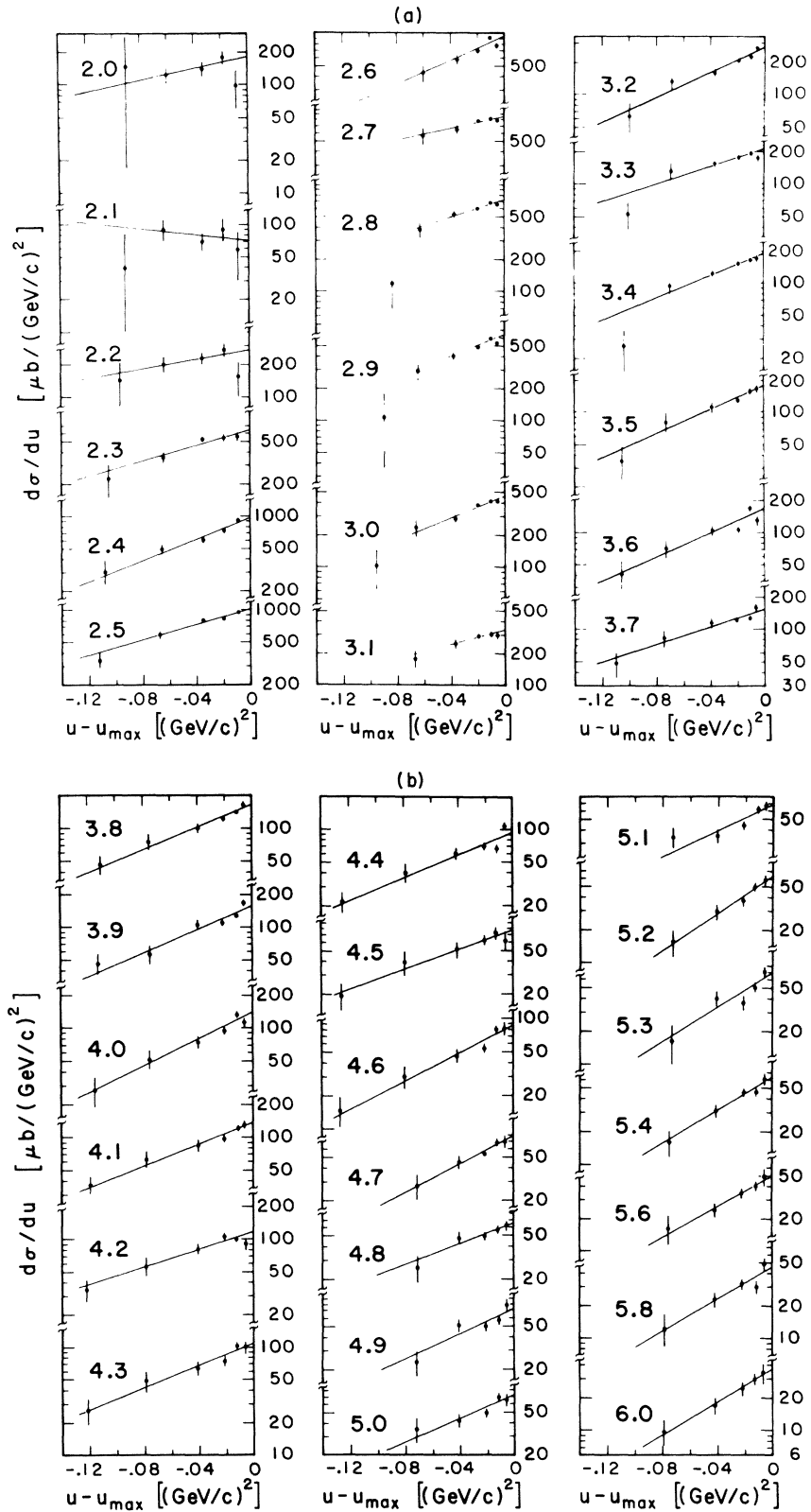


FIG. 4. Angular distributions obtained in the  $\theta^B$  analysis. The straight-line fits were generated in program BAKFIT.

TABLE V. Comparison of slopes and intercepts for the two spectrometer geometries. The low-momentum geometry (*L*) included momenta from 2.0 to 4.6 GeV/*c* and the high-momentum geometry (*H*) ranged from 4.4 to 6.0 GeV/*c*. The two momenta studied at both geometries were 4.4 and 4.6 GeV/*c*.

Momentum (GeV/ <i>c</i> )	Analysis	Spectrometer geometry	$d\sigma/d\Omega(180^\circ)$ ( $\mu\text{b}/\text{sr}$ )	Slope [(GeV/ <i>c</i> ) <sup>-2</sup> ]
4.4	$\theta^B$	<i>L</i>	$56.5_{-3.3}^{+3.5}$	$12.1 \pm 1.8$
		<i>H</i>	$58.4_{-4.9}^{+5.3}$	$15.9 \pm 4.1$
4.4	$\theta^F$	<i>L</i>	$58.3_{-3.7}^{+3.9}$	$12.1 \pm 1.6$
		<i>H</i>	$58.5_{-5.4}^{+6.0}$	$15.5 \pm 4.0$
4.6	$\theta^B$	<i>L</i>	$55.0_{-4.1}^{+4.4}$	$14.9 \pm 2.3$
		<i>H</i>	$48.7_{-3.7}^{+4.0}$	$14.8 \pm 3.5$
4.6	$\theta^F$	<i>L</i>	$54.6_{-4.8}^{+5.3}$	$14.5 \pm 2.1$
		<i>H</i>	$48.8_{-4.3}^{+4.7}$	$13.9 \pm 3.6$

That is, in the resonance model it is assumed that the scattering mechanism involves resonance formation in the direct channel, and the energy dependence of the backward cross section is expected to exhibit structure because the probability of resonance formation is intimately related to the total amount of available center-of-mass energy. On the other hand, the Regge model has had some success in explaining the dip in the  $\pi^+p$  elastic differential cross section at  $u \sim -0.15$  (GeV/*c*)<sup>2</sup> by assuming that the scattering mechanism involves the crossed-channel exchange of the *N* and  $\Delta$  Regge trajectories. For this reason, in the interference model it is assumed that the backward scattering amplitude includes both the direct- and cross-channel mechanisms, as is illustrated

in Fig. 8. However, there is still some question as to how to take into account the contributions from both mechanisms. It has been pointed out<sup>11, 12</sup> that an amplitude written as a simple sum of Breit-Wigner amplitudes and a full Regge amplitude can involve double counting. For the case of  $\pi^+p$  backward elastic scattering a solution to this problem was proposed by Ma and Shaw.<sup>13</sup> They identify the sum of the direct-channel resonances with the signed part of the Regge amplitude and associate the purely real, nonsigned part with an interfering background. Thus, they write the scattering amplitude as a sum of Breit-Wigner amplitudes and only the nonsigned part of the Regge amplitude. The 180° cross sections obtained in this experiment (Table VI and Fig. 6)

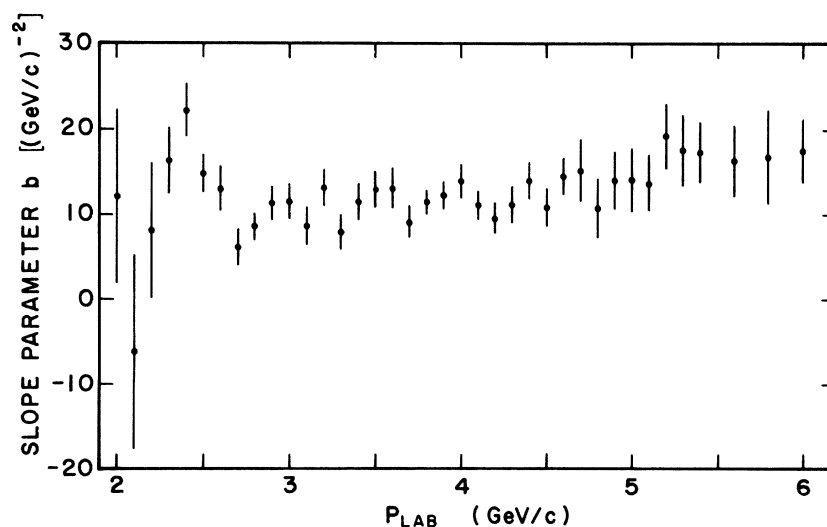


FIG. 5. Momentum dependence of the slope of the backward peak in  $\pi^+p$  elastic scattering. These are the averages of the slopes obtained in the  $\theta^B$  and  $\theta^F$  analyses.

TABLE VI. Slope parameters and differential cross sections at  $180^\circ$  for  $\pi^+ p$  backward elastic scattering.

$P_\pi$ (GeV/c)	$\sqrt{s}$ (MeV)	$\frac{d\sigma}{d\Omega}$ ( $180^\circ$ ) ( $\mu\text{b}/\text{sr}$ )	$\frac{d\sigma}{du}$ ( $180^\circ$ ) [ $\mu\text{b}/(\text{GeV}/c)^2$ ]	Slope [ $(\text{GeV}/c)^{-2}$ ]
2.0	2159	$44.0^{+10.1}_{-8.2}$	$183^{+42}_{-34}$	$12.1 \pm 10.2$
2.1	2202	$18.3^{+6.0}_{-4.5}$	$74^{+24}_{-18}$	$-6.2 \pm 11.5$
2.2	2244	$71.5^{+14.5}_{-12.1}$	$266^{+54}_{-45}$	$8.1 \pm 8.0$
2.3	2286	$181.2^{+15.6}_{-14.6}$	$638^{+55}_{-51}$	$16.3 \pm 3.9$
2.4	2326	$291.9^{+16.5}_{-15.5}$	$979^{+55}_{-52}$	$22.2 \pm 3.2$
2.5	2366	$307.2^{+14.7}_{-14.3}$	$982^{+47}_{-46}$	$14.8 \pm 2.3$
2.6	2405	$312.6^{+19.5}_{-17.4}$	$955^{+57}_{-53}$	$13.0 \pm 2.7$
2.7	2444	$289.6^{+13.1}_{-12.6}$	$847^{+38}_{-37}$	$6.2 \pm 2.1$
2.8	2482	$255.5^{+6.6}_{-6.5}$	$716^{+19}_{-18}$	$8.5 \pm 1.5$
2.9	2520	$228.2^{+10.1}_{-9.2}$	$615^{+27}_{-25}$	$11.3 \pm 2.0$
3.0	2556	$177.7^{+9.0}_{-8.4}$	$460^{+23}_{-22}$	$11.6 \pm 2.0$
3.1	2592	$135.2^{+8.6}_{-8.1}$	$337^{+21}_{-20}$	$8.7 \pm 2.3$
3.2	2628	$116.2^{+6.3}_{-6.1}$	$280^{+15}_{-15}$	$13.2 \pm 2.1$
3.3	2664	$89.3^{+5.6}_{-5.3}$	$208^{+13}_{-12}$	$7.9 \pm 2.1$
3.4	2699	$85.0^{+5.3}_{-5.0}$	$191^{+12}_{-11}$	$11.5 \pm 2.2$
3.5	2733	$83.8^{+5.3}_{-4.9}$	$182^{+12}_{-11}$	$13.0 \pm 2.1$
3.6	2767	$81.2^{+6.0}_{-5.5}$	$171^{+13}_{-12}$	$13.1 \pm 2.4$
3.7	2801	$74.9^{+4.7}_{-4.4}$	$153^{+10}_{-9}$	$9.2 \pm 1.9$
3.8	2834	$83.0^{+3.4}_{-3.3}$	$165^{+7}_{-7}$	$11.5 \pm 1.4$
3.9	2867	$83.3^{+3.7}_{-3.7}$	$161^{+7}_{-7}$	$12.3 \pm 1.6$
4.0	2900	$74.8^{+5.3}_{-4.8}$	$140^{+10}_{-9}$	$14.0 \pm 2.0$
4.1	2932	$75.4^{+4.1}_{-3.9}$	$138^{+7}_{-7}$	$11.2 \pm 1.7$
4.2	2964	$66.6^{+4.4}_{-4.2}$	$118^{+9}_{-8}$	$9.6 \pm 1.8$
4.3	2995	$62.3^{+5.0}_{-4.7}$	$108^{+9}_{-8}$	$11.2 \pm 2.0$
4.4	3026	$57.8^{+3.2}_{-3.0}$	$97.6^{+5.4}_{-5.0}$	$13.9 \pm 2.2$
4.5	3057	$48.8^{+5.0}_{-4.6}$	$80.4^{+8.2}_{-7.6}$	$10.9 \pm 2.3$
4.6	3088	$51.8^{+3.0}_{-2.8}$	$83.3^{+4.8}_{-4.5}$	$14.5 \pm 2.1$
4.7	3118	$50.7^{+4.6}_{-4.3}$	$79.6^{+7.2}_{-6.8}$	$15.2 \pm 3.7$
4.8	3148	$43.2^{+4.1}_{-3.9}$	$66.3^{+6.3}_{-6.0}$	$10.8 \pm 3.5$
4.9	3177	$50.4^{+5.0}_{-4.6}$	$75.7^{+7.5}_{-6.9}$	$14.1 \pm 3.4$
5.0	3207	$52.3^{+4.7}_{-4.3}$	$76.8^{+6.9}_{-6.3}$	$14.2 \pm 3.8$
5.1	3236	$47.9^{+4.1}_{-3.7}$	$68.8^{+5.9}_{-5.3}$	$13.7 \pm 3.4$
5.2	3265	$44.7^{+4.3}_{-3.9}$	$62.9^{+6.0}_{-5.4}$	$19.3 \pm 3.8$
5.3	3293	$50.7^{+5.1}_{-4.9}$	$69.9^{+7.0}_{-6.8}$	$17.5 \pm 4.3$
5.4	3322	$47.6^{+4.6}_{-4.3}$	$64.3^{+6.2}_{-5.8}$	$17.3 \pm 3.6$
5.6	3378	$38.7^{+4.7}_{-4.1}$	$50.3^{+6.1}_{-5.3}$	$16.3 \pm 4.2$
5.8	3433	$38.2^{+4.6}_{-4.1}$	$47.8^{+5.8}_{-5.1}$	$16.8 \pm 5.5$
6.0	3487	$30.9^{+4.3}_{-3.7}$	$37.3^{+5.2}_{-4.5}$	$17.5 \pm 3.9$

were interpreted using both a pure resonance model and an interference model similar to that of Ma and Shaw.

### B. The resonance model

The spin-nonflip and -flip parts of the resonance amplitude were parameterized as follows:

$$(\text{spin-nonflip})F_{\text{res}} = \frac{1}{k} \sum_n \frac{C_n X_n (J_n + \frac{1}{2})}{\epsilon_n - i} P_l(\cos\theta), \quad (1)$$

$$(\text{spin-flip})G_{\text{res}} = \frac{1}{k} \sum_n \frac{C_n X_n (-1)^{J_n - l + 1/2}}{\epsilon_n - i} \times \frac{dP_l(\cos\theta)}{d(\cos\theta)}, \quad (2)$$

where  $k$  is the center-of-mass momentum,  $C_n$  is a Clebsch-Gordan coefficient which equals 1 for  $\pi^+ p$  resonances,  $\theta$  is the center-of-mass scattering angle,  $J_n$  is the spin of the resonance,  $X_n$  is its elasticity,  $\epsilon_n = (M_n^2 - s)/M_n \Gamma_n$ ,  $s$  is the square of the energy in the center-of-mass system,  $M_n$  is the mass of the resonance, and  $\Gamma_n$  is its full width. The effects of the Breit-Wigner tails for

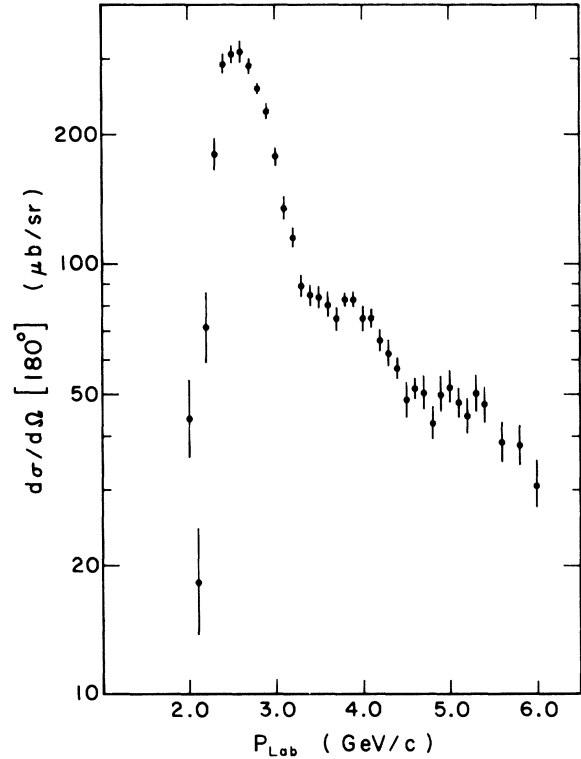


FIG. 6. Momentum dependence of the  $180^\circ$  differential cross section in  $\pi^+ p$  elastic scattering. These are the averages of the intercepts obtained in the  $\theta^F$  and  $\theta^B$  analyses.

each resonance at mass values far away from  $M_n$  were decreased by multiplying each resonance amplitude by the factor  $\exp(-d\epsilon_n^2)$ , where  $d$  is a dimensionless cutoff parameter. This approach to reducing the resonance tails is similar to that described in Ref. 14. Figure 9 illustrates the effect of this factor on a Breit-Wigner curve for the  $\Delta(2850)$  resonance.

### C. The interference model

Following a procedure used by other authors<sup>15, 16</sup> Ma and Shaw<sup>17</sup> write the spin-nonflip and -flip parts of the Regge amplitude for pion-nucleon scattering as

$$(\text{spin-nonflip})F_{\text{Reg}}(\sqrt{s}, u) = \sum_j [f_j(\sqrt{s}, u) - (\cos\theta)f_j(-\sqrt{s}, u)], \quad (3)$$

$$(\text{spin-flip})G_{\text{Reg}}(\sqrt{s}, u) = \sum_j f_j(-\sqrt{s}, u), \quad (4)$$

where the summation is taken over the  $N$  and  $\Delta$

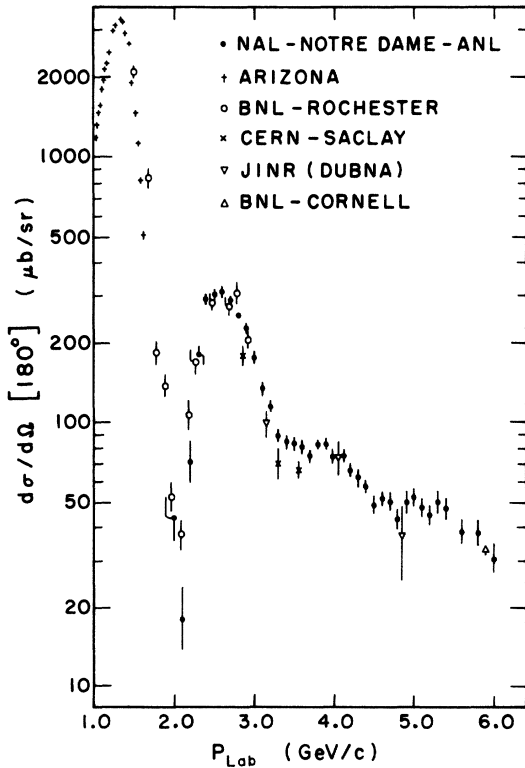


FIG. 7. Momentum dependence of the  $180^\circ$  differential cross section in  $\pi^+p$  elastic scattering. The data from Fig. 6 are shown with data from Arizona (Ref. 9), BNL-Rochester (Ref. 1), CERN-Saclay (Ref. 2), JINR (Ref. 3), and BNL-Cornell (Ref. 4).

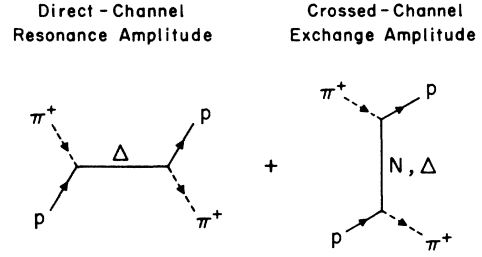


FIG. 8. Schematic representation of the direct-channel and crossed-channel amplitudes. The resonance model includes only the direct channel, but the interference model includes contributions from both amplitudes.

trajectories. The crossing symmetry relation, which relates the amplitude  $g_j(\sqrt{u}, s)$  for the  $j$ th Regge trajectory to the amplitude  $f_j(\sqrt{s}, u)$ , is given by

$$f_j(\pm\sqrt{s}, u) = \frac{0.5(E_s^+ + M)}{\pm\sqrt{s}} \times \left[ \frac{(\sqrt{u} \mp \sqrt{s} + 2M)}{E_u + M} g_j(\sqrt{u}, s) + \frac{(\sqrt{u} \pm \sqrt{s} - 2M)}{E_u - M} g_j(-\sqrt{u}, s) \right], \quad (5)$$

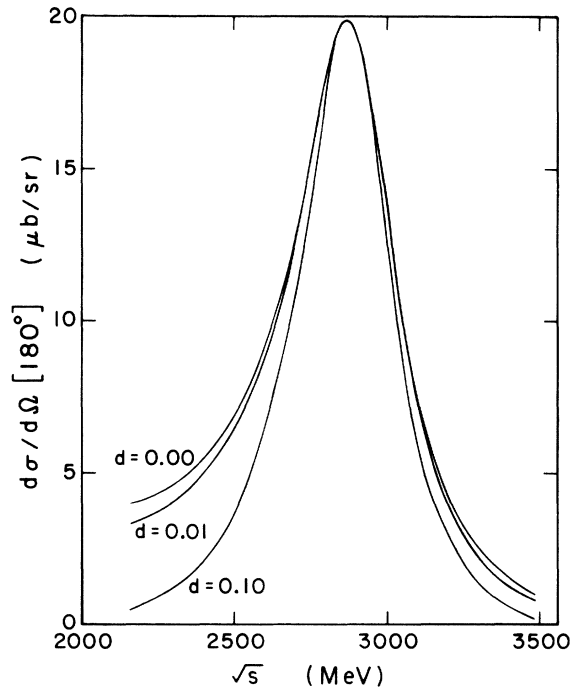


FIG. 9. Breit-Wigner curve for the  $\Delta(2850)$  using three different values for the exponential damping factor  $d$ . For this calculation the  $\Delta(2850)$  was assigned a mass of  $2889 \text{ MeV}/c^2$  and a full width of  $406 \text{ MeV}/c^2$ . The product  $X(J + \frac{1}{2})$  was taken to be 0.29.

where  $E_s^\pm = 0.5(s + M^2 - \mu^2)/(\pm\sqrt{s})$  and a corresponding definition holds for  $E_u$ . The masses of the proton and pion are represented by  $M$  and  $\mu$ , respectively. The explicit form for  $g_j(\pm\sqrt{u}, s)$  is

$$g_j(\pm\sqrt{u}, s) = \frac{\gamma_j^\pm}{\pm\sqrt{u}} \frac{(E_u \pm M)[1 + \tau_j e^{-i\pi(\alpha_j^\pm - 1/2)}]}{\Gamma(\alpha_j^\pm + \frac{1}{2}) \cos \pi \alpha_j^\pm} \times \left(\frac{s}{s_j}\right)^{\alpha_j^\pm - 1/2}, \quad (6)$$

where the  $\alpha_j$ ,  $\gamma_j$ , and  $s_j$  are parameterized as<sup>18</sup>

$$\begin{aligned} \gamma_N^\pm &= \mp 11.7(1 \mp 1.25\sqrt{u}) \text{ GeV}^{-1}, \\ \alpha_N^\pm &= -0.35 \pm 0.09\sqrt{u} + 1.07u, \\ s_N &= 1.0 \text{ GeV}^2, \\ \gamma_\Delta^\pm &= \pm 0.186(1 \pm 1.6\sqrt{u}) \text{ GeV}^{-1}, \\ \alpha_\Delta^\pm &= +0.14 + 0.89u, \\ s_\Delta &= +1.7 \text{ GeV}^2. \end{aligned}$$

The signature factor  $\tau_j$  is  $-1$  for the  $\Delta$  trajectory and  $+1$  for the  $N$  trajectory. The term containing this factor is called the signatured part of the amplitude. It is not used in the interference model

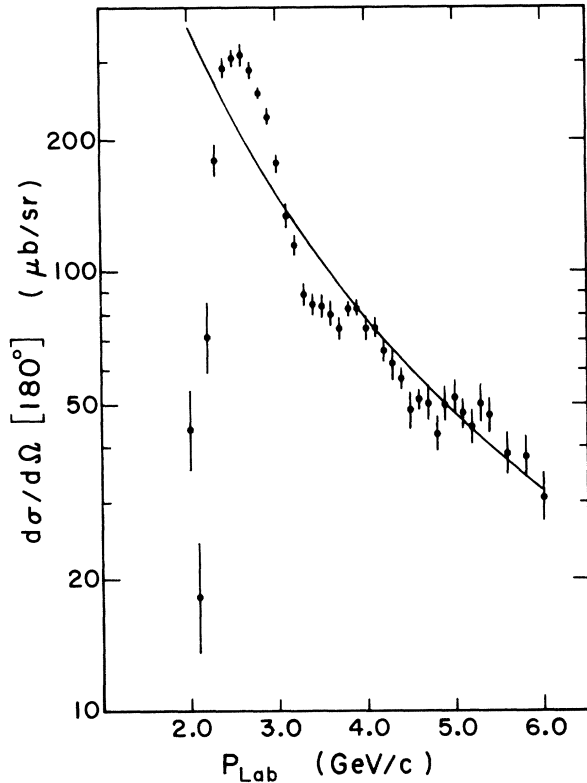


FIG. 10. Comparison of the data with the total Regge-model cross section including both the signatured and nonsignatured parts of the Regge amplitude using the fixed parameters listed in Sec. IV C.

but is included here so that a comparison may be made between a fit obtained using only the total Regge amplitude and those obtained using the interference model amplitudes. The former fit has a smooth energy dependence and fits the data only in an average sense, as is shown in Fig. 10. It is clear that the Regge amplitude alone cannot account for the structure observed in this energy region. Much better fits to the data were obtained by eliminating the signatured part of the Regge amplitude and writing the total amplitude as a sum of the nonsignatured part of the Regge amplitude and the resonance amplitudes described in Sec. IV B. This elimination of the signatured term is the defining characteristic of the interference model of Ma and Shaw, which is based on the assumption that the signatured part can be identified with the sum of the direct-channel resonances. One may include the contribution of these resonances either by parameterizing them in terms of their Breit-Wigner amplitudes or by including the signatured term in the Regge amplitude. Inclusion of both the signatured term and the Breit-Wigner amplitudes would involve double counting. Thus, the total interference-model amplitude used in making the fits described below included contributions from (1) and (2) as well as (3) and (4):

$$\frac{1}{(\hbar c)^2} \frac{d\sigma}{d\Omega} = (F_{\text{res}} + F_{\text{Reg}}^{\text{ns}})^2 + \sin^2\theta (G_{\text{res}} + G_{\text{Reg}}^{\text{ns}})^2, \quad (7)$$

where the superscript "ns" on the Regge amplitudes indicates that they were calculated using only the contribution from the nonsignatured term.

#### D. Method of fitting

A multiparameter maximum-likelihood fitting program was used to fit the data shown in Fig. 6. The fit parameters were the parameters of the  $\Delta^{++}$  resonances having masses between 2170 and 3490 MeV/c<sup>2</sup>. The parameters for the nonsignatured part of the Regge amplitude used in the interference model fits were not varied. The contribution from this amplitude was calculated using the method and parameterization described in Sec. IV C. Because the fits were restricted to the values of  $d\sigma/d\Omega$  at  $180^\circ$ , the values for  $P_i(\cos\theta)$  reduced to  $\pm 1$ , depending on the parity of the resonances. Thus, in Eq. (1) it was possible to vary the product  $X_n(J_n + \frac{1}{2})$  in order to obtain a fit but no additional information could be obtained about the separate values of  $X_n$  and  $J_n$ . The spin-flip amplitudes (2) and (4) do not contribute to the amplitude at  $180^\circ$ , so they were not considered in making these fits, but they were included in a separate investigation of the slope

TABLE VII. Resonance parameters from the Particle Data Group listings used as input to the fitting program. Parameters of resonances above  $2160 \text{ MeV}/c^2$  were allowed to vary. All others remained fixed.

	Classification <sup>a</sup>	$J^P$	Mass ( $\text{MeV}/c^2$ )	Width ( $\text{MeV}/c^2$ )	$X(J + \frac{1}{2})$
A. Data fixed in fitting process					
$\Delta(1236)$	****	$\frac{3}{2}^+$	1233	116	$0.994 \times 2$
$\Delta(1650)$	****	$\frac{1}{2}^-$	1637	165	$0.29 \times 1$
$\Delta(1670)$	***	$\frac{3}{2}^-$	1685	245	$0.15 \times 2$
$\Delta(1690)$	*	$\frac{3}{2}^+$	1710	324	$0.10 \times 2$
$\Delta(1890)$	***	$\frac{5}{2}^+$	1877	259	$0.17 \times 3$
$\Delta(1910)$	***	$\frac{1}{2}^+$	1889	305	$0.25 \times 1$
$\Delta(1950)$	****	$\frac{7}{2}^+$	1947	199	$0.44 \times 4$
$\Delta(1960)$	*	$\frac{5}{2}^-$	2018	437	$0.14 \times 3$
$\Delta(2160)$	*	$\frac{3}{2}^+$	2155	230	$0.28 \times 2$
B. Data varied in fitting process					
$\Delta(2200)$	Not listed				
$\Delta(2420)$	***	$\frac{11}{2}^+$	2320–2450	270–350	$0.11 \times 6$
$\Delta(2850)$	***	? <sup>+</sup>	~2850	~400	0.25
$\Delta(3230)$	***	?	~3230	~440	0.05

<sup>a</sup>\*\*\*\*Good, clear, and unmistakable. \*\*\*Good, but in need of clarification or not absolutely certain. \*\*Needs confirmation. \*Weak.

parameters.

The input resonance masses, widths, elasticities, spins, and parities were taken from the Particle Data Group listings<sup>19</sup> and are shown in Table VII. Because resonances labeled with one star are not well established, fits were made both including and excluding the one-star resonances. In either case the parameters describing the resonances with masses below  $2170 \text{ MeV}/c^2$  were held fixed, while those corresponding to masses above  $2170 \text{ MeV}/c^2$  were allowed to vary until a good fit to the data was obtained.

Considerable attention was given to fitting the dip near  $2.1 \text{ GeV}/c$ . Several attempts were made to obtain a fit without introducing a new negative-parity  $\Delta$  resonance. The effect of the cutoff parameter  $d$  was studied carefully because it was thought that the dip could be simply a valley between two positive-parity resonances. If this were true and if the tails of the resonances were effectively eliminated by choosing an appropriately large value for  $d$ , it would be possible to fit the dip without using a negative-parity resonance. However, this approach proved to be unsuccessful because it soon became clear that a value of  $d$

large enough to fit the dip at  $2.1 \text{ GeV}/c$  would be too large to allow a reasonable fit in the regions near  $3.6 \text{ GeV}/c$  and  $4.7 \text{ GeV}/c$ . Another approach to fitting the dip involved studying the effects of the one-star resonances. It was conjectured that the inclusion or exclusion of the  $\Delta(1960)$  and  $\Delta(2160)$  could have an appreciable effect in the dip region. However, attempts to fit the data without including a negative-parity resonance at  $\sim 2200 \text{ MeV}/c^2$  were unsuccessful, regardless of whether or not the  $\Delta(1960)$  and  $\Delta(2160)$  were included. In fact, for both the resonance and interference models, the values of the  $\chi^2$  for fits excluding the  $\Delta(2200)$  were never better than 400 for 29 degrees of freedom, regardless of the choice of  $d$ , or the inclusion of the one-star resonances. On the other hand, when the  $\Delta(2200)$  was included<sup>20–24</sup> all of the aforementioned variations in the approach to fitting gave good fits to the dip at  $2.1 \text{ GeV}/c$ . A study of these variations for each of the two models has been presented elsewhere.<sup>6</sup> Because no new physical insight is to be gained by reconsidering these variations, the remainder of this paper is restricted to a discussion of fits obtained with  $d=0.01$  and with the one-star resonances included.

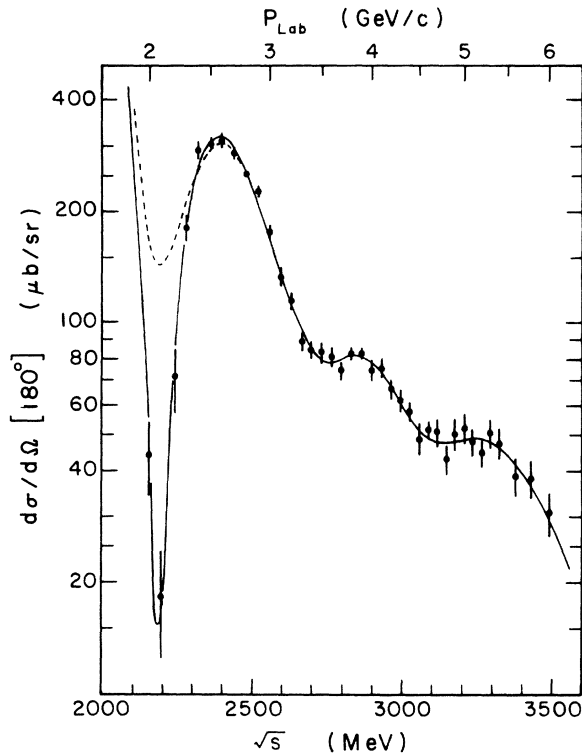


FIG. 11. Resonance-model fit to the data. It is not significantly different from the interference-model fit.

Attention was also given to fitting in the region near 5 GeV/c because of the uncertainty introduced by the lack of information on the resonance structure above 6.0 GeV/c. The  $\Delta(3230)$  is the fifth recurrence on a Regge trajectory which also includes the  $\Delta(1236)$ ,  $\Delta(1950)$ ,  $\Delta(2420)$ , and  $\Delta(2850)$ . The sixth recurrence has not been observed, but its parameters can be inferred by extrapolation.<sup>14</sup> Hence, the existence of a sixth

TABLE VIII. Comparison of the results of fitting using the resonance (R) and interference (I) models. For each parameter two values are presented, one for the resonance-model fit and one for the interference-model fit. The  $\chi^2$  for both models was 16 for 26 degrees of freedom.

Model	Mass (MeV/c <sup>2</sup> )	Width (MeV/c <sup>2</sup> )	$X(J + \frac{1}{2})$	
$\Delta(2200)$	R	$2182^{+31}_{-26}$	$279 \pm 120$	$1.08^{+0.26}_{-0.21}$
	I	$2226^{+14}_{-22}$	$291^{+130}_{-81}$	$0.75^{+0.45}_{-0.11}$
$\Delta(2420)$	R	$2390 \pm 48$	$483 \pm 75$	$1.00^{+0.37}_{-0.16}$
	I	$2473^{+65}_{-85}$	$467 \pm 113$	$0.61^{+0.40}_{-0.20}$
$\Delta(2850)$	R	$2877^{+21}_{-23}$	$358^{+120}_{-180}$	$0.27^{+0.12}_{-0.18}$
	I	$2960 \pm 44$	$258^{+322}_{-114}$	$0.13^{+0.10}_{-0.05}$
$\Delta(3230)$	R	$3269^{+55}_{-55}$	$644^{+1000}_{-280}$	$0.40^{+0.04}_{-0.08}$
	I	$3421^{+150}_{-70}$	$503^{+2720}_{-230}$	$0.12^{+0.18}_{-0.12}$

recurrence was hypothesized and its parameters were included in the fixed input to the fitting program for the resonance model. The difference between the best fit parameters for fits including and excluding the sixth recurrence was not significant. Using the resonance model a good fit in the 5 GeV/c region could not be achieved without including the  $\Delta(3230)$ .

#### E. Results of fitting

The curve shown in Fig. 11 is the resonance-model fit to the data; it is not significantly different from the interference-model fit. The dashed line in this figure illustrates the best fit possible if the  $\Delta(2200)$  is excluded. Table VIII lists the best fit parameters for both models.<sup>25</sup> The statistical error on a given parameter was obtained by perturbing that parameter about its optimal value and refitting the remaining parameters. This process was continued until the  $\chi^2$  of the new fit differed from that of the best fit by an amount corresponding to one standard deviation.<sup>26</sup>

The parameters obtained for the pure resonance

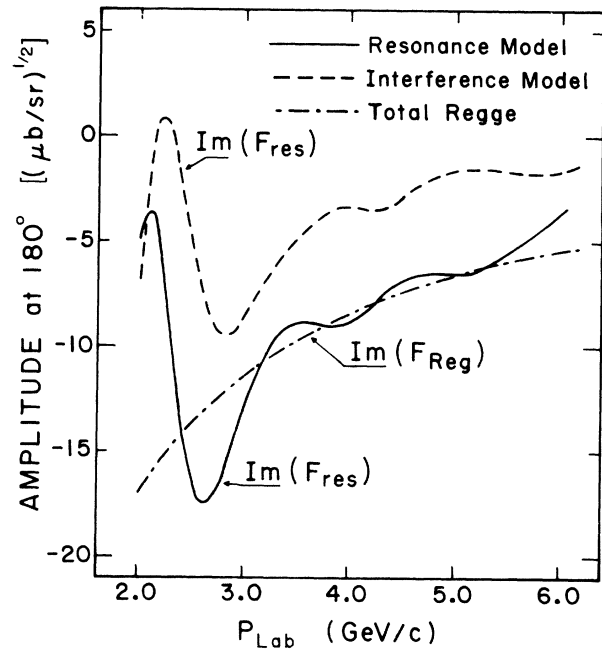


FIG. 12. Imaginary part of the  $\pi^+p$  scattering amplitude for the resonance model (solid curve) and interference model (dashed curve). These curves were obtained from fits which included the one-star resonances and had a cutoff,  $d=0.01$ . The nonsignatured part of the Regge amplitude used in the interference model has no imaginary part. The imaginary part of the total Regge amplitude which arises from the signatured part of Eq. (6) is shown by the dot-dashed curve using the fixed parameters listed in Sec. IV C.

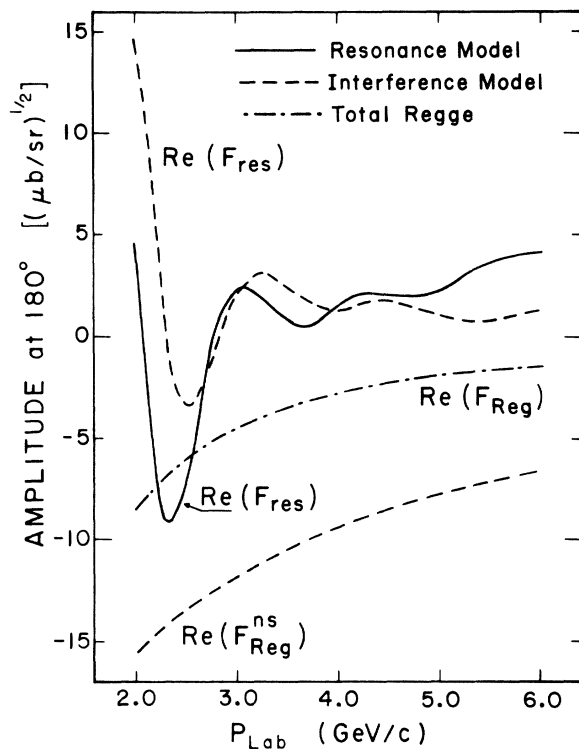


FIG. 13. Real part of the  $\pi^+p$  scattering amplitude for the resonance model (solid curve) and interference (upper dashed curve) model. These curves were obtained from fits which included the one-star resonances and had a cutoff,  $d=0.01$ . The lower dashed curve shows the contribution from the nonsignatured part of the Regge amplitude as used in the interference model. The dot-dashed curve shows the contributions from the total Regge amplitude, including both the signatured and nonsignatured parts.

model differ from those of the interference model. For example, the products  $X(J+\frac{1}{2})$  are larger in the resonance model. A comparison of the amplitudes contributing to the  $180^\circ$  cross section in each model is given in Fig. 12 for the imaginary parts and in Fig. 13 for the real parts. Both models can be made to fit the data with no significant difference in either the goodness of fit or the predicted

energy dependence of the cross section. The values of the parameters obtained by these two models differ somewhat; the Particle Data Group averages<sup>27</sup> are based on results which were obtained from methods most consistent with the resonance-model interpretation. However, fits based on both models require the inclusion of a negative-parity resonance at  $\sim 2200$  MeV. Additional evidence for the existence of a  $\Delta(2200)$  was obtained by substituting the best fit parameters into Eqs. (1) to (6), using only the nonsignatured part of (6) and predicting a slope parameter for each of the incident pion momenta. For both models the structure observed in Fig. 5 between 2.0 and 2.5 GeV/c could be produced only when the  $\Delta(2200)$  was included.

## V. SUMMARY

Differential cross sections for backward elastic  $\pi^+p$  scattering were measured from 2 to 6 GeV/c. These cross sections were extrapolated to  $180^\circ$  and the resulting values were fit using a resonance model and an interference model. Both models led to good fits to the data and yielded values for the masses, widths, parities, and the product of spin and elasticity for the  $\Delta(2200)$ ,  $\Delta(2420)$ ,  $\Delta(2850)$ , and  $\Delta(3230)$  resonances. Our data confirm the existence of the  $\Delta(3230)$  and require a negative parity  $\Delta(2200)$ .

## ACKNOWLEDGMENTS

We wish to thank our former collaborator, Dr. George Burlison, for his participation in the preparatory phases of this experiment, Dr. David Thomas for his help during the data-taking phase, Dr. David Carey for TURTLE software, and Ron Erichsen, Cordon Kerns, William Rickhoff, and Hoshang Vaid for their technical assistance. It is a pleasure to thank the entire staff at the Argonne ZGS for their advice and help throughout this experiment, and the University of Notre Dame Computing Center for their aid in the data analysis phase.

\*Present address: Fermi National Accelerator Laboratory, Batavia, Ill. 60510.

†Present address: Physics Department, University of California, Los Angeles, Calif. 90024.

‡Work supported in part by the National Science Foundation.

§Present address: Max-Planck-Institut für Physik und Astrophysik, München, West Germany.

||Work supported by the U. S. Atomic Energy Commission.

<sup>1</sup>A. S. Carroll, J. Fischer, A. Lundby, R. H. Phillips, C. L. Wang, F. Lobkowitz, A. C. Melissinos, Y. Nagashima, and S. Tewksbury, *Phys. Rev. Lett.* **20**, 607 (1968).

<sup>2</sup>W. F. Baker, P. J. Carlson, V. Chabaud, A. Lundby, J. Banaigs, J. Berger, C. Bonnel, J. Duflo, L. Goldzahl, and F. Plouin, *Nucl. Phys.* **B9**, 249 (1969).

<sup>3</sup>A. S. Vovenko, B. N. Gus'kov, M. F. Likhachev, A. L. Lyubimov, Yu. A. Matulenko, I. A. Savin, and V. S.

- Stavinskii, Zh. Eksp. Teor. Fiz. Pis'ma Red. 2, 409 (1965) [JETP Lett. 2, 255 (1965)].
- <sup>4</sup>D. P. Owen, F. C. Peterson, J. Orear, A. L. Read, D. G. Ryan, D. H. White, A. Ashmore, C. J. S. Damerell, W. R. Frisken, and R. Rubinstein, Phys. Rev. 181, 1794 (1969).
- <sup>5</sup>W. F. Baker, D. P. Eartly, K. P. Pretzl, S. M. Pruss, A. A. Wehmann, P. Koehler, A. J. Lennox, J. A. Poirier, C. A. Rey, and O. R. Sander, Phys. Rev. Lett. 32, 251 (1974).
- <sup>6</sup>C. A. Rey, A. J. Lennox, J. Poirier, and K. P. Pretzl, Phys. Rev. Lett. 32, 908 (1974); 33, 250 (1974).
- <sup>7</sup>K. L. Brown and S. K. Howry, SLAC Report No. SLAC-91, 1970 (unpublished).
- <sup>8</sup>D. C. Carey, NAL Report No. NAL-64, 1971 (unpublished).
- <sup>9</sup>R. E. Rothschild, T. Bowen, P. K. Caldwell, D. Davidson, E. W. Jenkins, R. M. Kalbach, D. V. Petersen, and A. E. Pifer, Phys. Rev. D 5, 499 (1972).
- <sup>10</sup>Additional information on  $\pi^+p$  backward elastic scattering in this energy range is to be found in papers by: M. Derrick, ANL Report No. ANL/HEP 6802, 1968 (unpublished); Particle Data Group, LBL Report No. LBL-63, 1973 (unpublished), part I; Aachen-Berlin-Birmingham-Bonn-Hamburg-London-München Collaboration, Phys. Lett. 10, 248 (1964); W. F. Baker, K. Berkelman, P. J. Carlson, G. P. Fisher, P. Fleury, D. Hartill, R. Kalbach, A. Lundby, S. Mukhin, R. Nierhaus, K. P. Pretzl, and J. Woulds, Nucl. Phys. B25, 385 (1971); A. Bashian, G. Finocchiaro, M. L. Good, P. D. Grannis, O. Guisan, J. Kirz, Y. Y. Lee, G. C. Fischer, and D. D. Reeder, Phys. Rev. D 9, 3193 (1974); H. Brody, R. Lanza, R. Marshall, J. Niederer, W. Selove, M. Shochet, and R. Van Berg, Phys. Rev. Lett. 18, 828 (1966); W. Busza, B. G. Duff, D. A. Garbutt, F. F. Heymann, C. C. Nimmon, K. M. Potter, T. P. Swetman, E. H. Bellamy, T. F. Buckley, R. W. Dobinson, P. V. March, J. A. Strong, and R. N. F. Walker, Phys. Rev. 180, 1339 (1969); C. T. Coffin, N. Dikmen, L. Ettlinger, D. Meyer, A. Saulys, K. Terwilliger, and D. Williams, *ibid.* 159, 1169 (1967); V. Cook, B. Cork, W. Holley, and M. L. Perl, *ibid.* 130, 762 (1963); D. E. Damouth, L. W. Jones, and M. L. Perl, Phys. Rev. Lett. 11, 287 (1963); L. Dick, Z. Janout, H. Aoi, C. Caverzasio, A. Gonidec, K. Kuroda, A. Michalowicz, M. Poulet, D. Sillou, D. G. Aschman, N. E. Booth, K. Green, and C. M. Spencer, Nucl. Phys. B43, 522 (1972); T. Dobrowolski, B. N. Gus'kov, M. F. Likhachev, A. L. Lubimov, Yu. A. Matulenko, V. S. Stavinsky, and A. S. Vovenko, Phys. Lett. 24B, 203 (1967); W. R. Frisken, A. L. Read, H. Ruderman, A. D. Krisch, J. Orear, R. Rubinstein, D. B. Scarl, and D. H. White, Phys. Rev. Lett. 15, 313 (1965); F. E. James, J. A. Johnson, and H. L. Kraybill, Phys. Lett. 19, 72 (1965); J. MacNaughton, W. R. Butler, D. G. Coyne, G. M. Hicks, and G. H. Trilling, Nucl. Phys. B33, 101 (1971); D. J. Schotanus, C. L. Pols, D. Z. Toet, R. T. Van de Walle, J. V. Major, G. E. Pearson, B. Chaurand, R. Vanderhaghen, G. Rinaudo, and A. E. Werbrouck, *ibid.* B22, 45 (1970); R. A. Sidwell, R. R. Crittenden, K. F. Galloway, R. M. Heinz, and H. A. Neal, Phys. Rev. D 3, 1523 (1971); S. S. Yamamoto and D. C. Rahm, Phys. Rev. 173, 1302 (1968).
- <sup>11</sup>C. B. Chiu and A. V. Stirling, Phys. Lett. 26B, 236 (1968).
- <sup>12</sup>R. Dolen, D. Horn, and C. Schmid, Phys. Rev. 166, 1768 (1968).
- <sup>13</sup>E. S. Ma and G. L. Shaw, Phys. Rev. D 3, 1264 (1971).
- <sup>14</sup>P. G. Tomlinson, R. A. Sidwell, D. B. Lichtenberg, R. M. Heinz, and R. R. Crittenden, Nucl. Phys. B25, 443 (1971).
- <sup>15</sup>V. Singh, Phys. Rev. 129, 1889 (1963).
- <sup>16</sup>V. Barger and D. Cline, Phys. Rev. 155, 1792 (1967).
- <sup>17</sup>E. Ma and G. L. Shaw (unpublished).
- <sup>18</sup>The apparent discrepancy between some of the signs shown here and those appearing in Ref. 13 is due to the use of different sign conventions. The Regge amplitudes used in our fits agree exactly with those calculated by Ma and Shaw (E. S. Ma and G. L. Shaw, private communication).
- <sup>19</sup>Particle Data Group, Phys. Lett. 39B, 1 (1972); see pp. 10, 93, 109, and 110.
- <sup>20</sup>Other investigators have suggested the existence of a negative-parity  $\Delta$  resonance having mass  $\sim 2200$  MeV/c. See Refs. 1, 13, 14, and 21-24.
- <sup>21</sup>W. Von Schlippe, Nuovo Cimento Lett. 4, 767 (1972).
- <sup>22</sup>J. L. Rosner, Phys. Rev. D 7, 172 (1973).
- <sup>23</sup>F. Wagner, paper presented at the XVI International Conference on High Energy Physics, Chicago-Batavia, 1972 (unpublished).
- <sup>24</sup>R. Shanta, Nuovo Cimento 70, 12 (1970).
- <sup>25</sup>The interference model parameters differ slightly from those of Ref. 6, where an approximation was used for the  $\gamma$  function and where  $\alpha_N^*$  had a slightly different parameterization.
- <sup>26</sup>This amount was calculated using the approximation that the quantity  $(2\chi^2)^{1/2} - (2n_D - 1)^{1/2}$  has unit standard deviation, where  $n_D$  is the number of degrees of freedom. See R. A. Fisher, *Statistical Methods for Research Workers* (Hafner, New York, 1970), p. 61.
- <sup>27</sup>Particle Data Group, Phys. Lett. 50B, 1 (1974).